Markus Franz Knoll

Development of a Low-cost, Wireless, Photoacoustic based NO_2 Recognition Sensor for Air Pollution Measurements

Master's Thesis

to achieve the university degree of
Master of Science

submitted to
Graz University of Technology

Supervisor
Univ.-Prof. Mag.rer.nat. Dr.rer.nat. Alexander Bergmann

Co-Supervisors
Ass.Prof. Dott. Dott. mag. Dr.techn. Carlo Alberto Boano, MSc
Dipl.-Ing. Philipp Breitegger, BSc

Institute of Electronic Sensor Systems

Graz, October 2018

This document is set in Palatino, compiled with pdfLaTeX2e and Biber.

The LaTeX template from Karl Voit is based on KOMA script and can be found online: https://github.com/novoid/LaTeX-KOMA-template

Affidavit

I declare that I have authored this thesis independently, that I have not used other than the declared sources/resources, and that I have explicitly indicated all material which has been quoted either literally or by content from the sources used. The text document uploaded to TUGRAZonline is identical to the present master's thesis.

Date	Signature

Preface

First of all I want to thank my supervisor Alexander Bergmann for the possibility to conduct the master thesis at the Institute of Electronic Sensor Systems. It was very interesting to design an own sensor and to get an insight into the different topics, in particular the physical part, which was quite new to me.

Further I want to thank Philipp Breitegger for the guidance and the vast amount of help he has provided through the thesis. Philipp helped me in specific with the construction of the cell, which he has accomplished. In addition, thanks a lot for helping me to improve my style of writing.

Many thanks to Benjamin Lang, who assisted me with the photoacoustic simulation.

I also want to thank Carlo Alberto Boano (Institute of Technical Informatics) for assisting me with the microcontroller platform and the LoRa application.

In addition, I want to thank my parents for giving me the opportunity to study and for the support, which they have always given to me.

Finally I want to particularly thank my girlfriend Eva, who has always motivated me and especially understood my limited amount of time during my study.

Zusammenfassung

Schlechte Luftqualität verursacht jährlich Millionen von frühzeitigen Todesfällen in Form von Atemwegs- oder Herzkreislauferkrankungen. Derzeit wird die Luftqualität nur in sehr geringer räumlicher Auflösung gemessen, was hauptsächlich den hohen Beschaffungs- und Wartungskosten von hochauflösenden Messgeräten geschuldet ist. Der derzeitige Trend ist der Einsatz von kostengünstigen Sensoren, die durch drahtlose Sensor-Technologien verbunden sind. Die Nachteile von kommerziell verfügbaren, kostengünstigen Geräten, sind vor allem die hohe Querempfindlichkeit zu anderen Schadstoffen, Langzeitabweichungen und eine hohe Sensibilität auf Umgebungseinflüsse wie Temperatur- oder Luftfeuchtigkeitsschwankungen.
In dieser Arbeit wird ein photoakustisch (engl. Photoacoustic, PA) basierender Stickstoffdioxid-Sensor, mit geringem Stromverbrauch und drahtloser Sensornetzwerkfähigkeit (engl. Wireless Sensor Network, WSN) vorgestellt. Das Sensorprinzip ist auf der photoakustischen-Spektroskopie (engl. Photoacoustic Spectroscopy, PAS) aufgebaut, mit der konkrete Schadstoffe detektiert werden können. Dies wird durch eine passende Auswahl des Absorptionsspektrums des jeweiligen Schadstoffes, beziehungsweise der Auswahl einer geeigneten Lichtquelle, ermöglicht.
Als Grundlage für den Sensor wurde eine photoakustische Zelle mit einem Qualitätsfaktor von 23 entworfen. Diese Zelle besteht aus zwei Resonatoren. Der erste Resonator wird durch die modulierte Leuchtdiode (engl. Light Emitting Diode, LED) angeregt. Der zweite Resonator misst das Hintergrundrauschen, um es nachfolgend zur Störsignalunterdrückung vom angeregten Signal abzuziehen. Dafür werden in dieser Arbeit speziell entwickelte Schaltungen mit geringem Stromverbrauch vorgestellt. Erstens, wird eine Schaltung vorgestellt, die das Modulationssignal der LED generiert, beziehungsweise das Referenzsignal für den Lock-In-Verstärker bereitstellt. Zweitens, werden zwei Schaltungen zur Verstärkung und Konvertierung

der beiden Mikrophonkanäle präsentiert. Außerdem werden Kalibrierungs-Software-Routinen zum Gleichanteil-, Verstärkungs-, und Phasenabgleich der beiden Mikrophonkanäle vorgestellt.
In der Folge, werden einerseits für die Detektion mittels des angeregten Resonators und andererseits für die Detektion unter Verwendung beider Resonatoren zur Störsignalunterdrückung, Ergebnisse präsentiert. Wobei Probleme mit der Phasenkalibrierung der beiden Mikrophonkanäle, eine erfolgreiche Verwendung beider Resonatoren zur Störsignalunterdrückung, verhinderten. Unter Verwendung des angeregten Resonators, konnte ein Detektionslimit von 101 ppb erreicht werden. Dabei wurde eine Integrationszeit von 124 s verwendet, beziehungsweise ein Stromverbrauch von 103 mA gemessen.
Ein flächendeckender Netzwerk-Sendeempfänger mit geringem Stromverbrauch (engl. Low Power Wide Area Network transceiver, LPWAN transceiver) wird verwendet, um die Daten nachfolgend an eine zentrale Sammelstelle zu übermitteln. Dabei wird im konkreten ein LoRa (engl. Long Range) Sendeempfänger eingesetzt. Bei den durchgeführten Distanzmessungen im städtischen Gebiet von Graz, wurden Kommunikationsdistanzen von mehr als 1.700 m erfolgreich bewältigt. Mit Hilfe dieser Erkenntnisse, kann der Einsatz von dichten Sensornetzen mit adäquater Sensor-Technologie zukünftig ermöglicht werden.

Abstract

Poor air quality causes millions of premature deaths, through respiratory or cardiovascular diseases. Currently, air pollution is monitored at low spatial resolution, mainly due to high acquisition and maintenance costs of appropriate measurement equipment. The current trend is the deployment of low-cost sensors, which are connected through wireless sensor network (WSN) technologies. However, those which are commercial available suffer from cross sensitivity, long term drift and dependency on environmental conditions.
In this work, a low-power, photoacoustic (PA) based nitrogen dioxide sensor with WSN capability is presented. The sensor principle is based on photoacoustic spectroscopy (PAS), which is able to detect specific pollutants. This is done through an appropriate selection of the absorption band of the pollutant and a corresponding light source.
As a foundation for the sensor, a differential photoacoustic cell with a quality factor of 23 was designed. The cell consists of two resonators. The first resonator is excited through a modulated light emitting diode (LED). The second resonator measures the background noise, to subsequently subtract it from the excited signal for noise cancellation. Therefor, special purpose, low-power circuits are presented in this work. Firstly, it features a signal generation circuit, which is used as modulation source for the LED and additionally features the reference signal for the implemented, hybrid lock-in amplifier (LIA). Secondly, two circuits for microphone signal amplification and conversion are introduced. In addition, to match the two microphone channels, software routines for offset, gain and phase calibration are proposed.
Results for single ended detection (excited resonator only) and differential detection (usage of both resonators for noise cancellation) are demonstrated, whereas issues within the phase calibration prevented successful usage of the differential detection. With the utilization of the single ended mode,

a limit of detection (LOD) down to 101 ppb could be achieved, with an integration time of 124 s and a power consumption of 103 mA.
A low-power wide-area network (LPWAN) long range (LoRa) transceiver is employed to transfer the acquired data to a central data sink. A communication range of more than 1.700 m in the urban area of Graz could be reached. This can enable dense sensor meshes with appropriate sensor technology for the future deployment of low-cost sensors.

Contents

List of Figures

1. Introduction

Poor air quality continues to be a threat for human health. Air quality issues gained attention in Europe through the "dieselgate" [1], whereby millions of premature deaths are caused, through respiratory or cardiovascular diseases [2].
Two different types of sources for air pollution exist. First, human made, or anthropogenic sources, are the main cause. These encompass contaminants created from road transport, industry, household or agriculture. Thereby, the main anthropogenic cause is fuel combustion. Second, natural sources comprise volcanic activities, pollen or desert dust.
The pollutants can be split into two categories. First particulate matter, measured in two different sizes. In particular PM_{10}, which are particles with diameters that are smaller than 10 μm and $PM_{2.5}$, particles smaller than 2.5 μm. Secondly, harmful gaseous compounds are monitored, including ozone (O_3), nitrogen dioxide (NO_2) and sulfur dioxide (SO_2). The world health organization (WHO) publishes each year annual reports, which represent the current situation of air pollution. Additionally, guidelines for short and long term limits are specified and reviewed. The current guideline for the mentioned pollutants is shown in Table 1.1. Currently, air pollution monitoring is performed only at very spatial resolution. In Austria, with a size of more than 83.000 km^2 and a population of nearly 9 million, 94 official air quality monitoring (AQM) stations are operated. This is roughly 1 station per 100.000 inhabitants or one site per 900 km^2 [3]. Less wealthy countries, like Senegal, operate only a handful of stations for millions of people. At the same time Senegal is the only country in West-Africa operating AQM sites [4]. This results in the strong need of increasing the density of air pollution monitoring.
The main issue is, the cost of the instruments and the expenditure for further equipment. Currently, research is going into the direction of the development of low-cost sensor equipment, to monitor air quality. Although a lot

of progress has been made in the last years, issues within this development exist. Sensor characteristics, like accuracy, stability, or the cross sensitivity to other pollutants, can not match up with the utilized AQM stations. In addition, as a consequence of a vast amount of sensors, the problem of connectivity and processing of the resulting bulk of data arises. One possible solution for connectivity is the utilization of low power wide area networks (LPWAN), to collect the data and transfer it to a central data sink.
Consequently, in this thesis, the development of a low-cost, wireless, photoacoustic based, nitrogen dioxide recognition sensor is presented. This sensor features on the one hand the capability to measure NO_2 and on the other hand provide the wireless network competence for transferring the data.
First, the background and the theoretical foundation of the used sensor principle, is provided in the following Chapter 2. Thereafter (Chapter 3), the sensor design is presented, first on system design level and consequently the individual blocks are described in detail. In the methodology section, the results of the laboratory evaluation of the sensor are demonstrated and discussed. Finally a conclusion and a short outlook of possible future work is given.

Pollutant	WHO guideline
$PM_{2.5}$	10 $\mu g/m^3$ annual mean 25 $\mu g/m^3$ daily mean
PM_{10}	20 $\mu g/m^3$ annual mean 50 $\mu g/m^3$ daily mean
O_3	100 $\mu g/m^3$ 8 hour mean
NO_2	40 $\mu g/m^3$ annual mean 200 $\mu g/m^3$ 1 hour mean
SO_2	20 $\mu g/m^3$ daily mean 500 $\mu g/m^3$ 10 minute mean

Table 1.1.: WHO guidelines [2] for particulate matter (PM), ozone (O_3), nitrogen dioxide (NO_2) and sulfur dioxide (SO_2).

2. Theoretical Background

In the previous introduction chapter, the foundation for the requirement of spatial dense air pollution measurement was provided. This chapter gives a theoretical insight into the developed sensor principle and the utilized sensor network component. Firstly, the required theoretical knowledge to the sensor basics is given and secondly, the sensor network foundation is provided.

2.1. Sensor Principles

The theoretical part about sensors mainly deals with the foundation of photoacoustic spectroscopy, which is the used principle of the later (cf. Chapter 3) described sensor design. Beforehand the following section discusses existing sensor technologies for the detection of environmental gases.

2.1.1. Sensor Technologies for Commercial Environmental Sensors

At present, the technologies for sensing environmental gases can mainly be split into two areas. The first group is high quality reference equipment. These instruments are certified to be used in legislative AQM stations and are therefore proofed to provide accurate analysis. Chemiluminescence or photoacoustic spectroscopy are two applied principles, which are used in these equipments. Currently AQM stations are very spatial deployed, due to high costs and regular calibration intervals of the instruments.
By contrast, the development of low cost air quality equipment is one of the

rising evolutions in the past years. Research is going into the direction to enhance the spatial resolution provided by the already used AQM stations. Currently though, most low cost sensor solutions achieve good results in laboratory environment, but deliver often strong deteriorated behavior in field measurements. The mainly used sensor principles to measure pollutants in the low cost area, are metal oxide semiconductor (MOS) and electrochemical (EC) based sensors.
MOS sensors measure the gas concentration based on changes in the resistance. The change of resistance occurs due to reduction or oxidation processes, dependent on the type of semiconductor (n-type, p-type) and the environmental gas. The resistance is mapped to the gas concentration through a non-linear response, which results into a complex conversion. MOS sensors suffer from cross sensitivity and are strongly impacted by temperature and humidity changes. As a result, frequent calibrations are necessary for different environmental conditions and to measure different types of gases. The long term employment (over several months) of MOS sensors is affected by a drift, which needs an additional calibration. Favorable aspects are the small sensors size, the fast response times and the relatively low detection limits. The power consumption is in the range of 100 mW, due to a required heating element. A more detailed theoretic introduction and practical results can be found in [5].
EC sensors detect the gas of interest through an electric current, proportional to the gas concentration. Typically they are built out of three electrodes (sensing electrode, reference electrode, counter electrode), which are separated by electrolyte. The gas diffuses through a small opening and reacts with the surface of the sensing electrode. The material of the electrode specifies, which gas should be detected. A resistor connected across the electrodes generates a proportional current according to the gas concentration. EC sensors require a small amount of power ($<$1 mW) to operate. They bring along small detection limits and have a linear response function. On the contrary, sensor drift as well as cross sensitivity are issues with EC sensors. Kumar et al. [6] provided a review of current environmental monitoring systems by representing several MOS and EC sensors for different gases. In [7], a literature summary of air quality sensors and recommendations for selecting sensor are provided. Existing sources mainly discuss the utilization of different MOS and EC sensors for gases and particular matter, with very different performance characteristics. In conclusion, they recommended

MOS sensors for O_3, NO_2 and CO and EC based sensors for sensing NO. Alastair et al. [8] evaluated low cost EC sensors in field employment and reported in particular issues with the interference calibrations. Especially the results of low cost EC NO_2 sensors compared to reference equipment showed very small correlation.

2.1.2. Photoacoustic Spectroscopy

After introducing existing sensor technologies, the following chapter pictures the fundamental theoretic foundations of the methodology part. The sensor design, which is described in Chapter 3, is based on photoacoustic spectroscopy (PAS). PAS utilizes the photoacoustic (PA) effect in the analysis of solid, liquid and gaseous compounds. This work only deals with spectroscopy of gases, in particular with the analysis of environmental gases. The focus is therefore on the spectroscopy of gases.

2.1.2.1. The Photoacoustic Effect and an Introduction to PAS

The photoacoustic effect was first discovered by A. G. Bell in 1880. During experiments with his photo-phone, he recognized an acoustic voice, while focusing an interrupted sun light beam onto a solid material.
Figure 2.1 illustrates the PA effect including the detection of the resulting wave. The PA effect can be triggered through a modulated light source, which excites molecules into higher energy states. The absorbed energy is subsequently released by a so-called relaxation process. The relaxation is split into two possible processes. On the one hand relaxation by radiation, which emits a photon through spontaneous, or induced emission. This process can usually be neglected in PAS, because the radiative lifetime is long compared to the deactivation through collision. On the other hand, relaxation through molecular collisions. Inelastic collisions of molecules convert the absorbed energy partly into heat. As a consequence, the modulation of the light source results into rapid temperature changes and these lead to a periodic pressure change of the system. This pressure change can be

measured by an acoustic sensitive device, for example a microphone (cf. [9]).

Figure 2.1.: Block diagram of photoacoustic spectroscopy. A modulated light source is used to excite molecules to enter higher energy states. This absorbed energy is subsequently transferred into kinetic energy. The movement of molecules causes inelastic collisions, which trigger a periodic heat change and consequently a periodical pressure change. This pressure change can be measured by an acoustic sensitive device.

Different light sources exist for PAS, like lasers or light emitting diodes (LED). Several selection criterias have to be considered, when choosing an appropriate light source. First, the wavelength (and bandwidth) must fit to the absorption spectrum of the gas of interest. Second, the cross sensitivity to other gases or particles must be taken to account, otherwise, the detected concentrations might be mistaken. An important aspect is the optical output power, which is proportional to the resulting sound pressure wave. Finally, the light source must be modulatable in the desired frequency range.
In most publications lasers are utilized, due to their high optical power and small radiation angle [10, 11, 12]. Nevertheless, publications exist, which used different types of LEDs as PA light sources [13, 14, 15]. Supplementary needs to be mentioned, that not only modulated (amplitude, wavelength) excitation can be applied. Another possibility is, to operate the light source in pulsed mode [16].
According to [17], the photoacoustic signal $S(\lambda)$ can be calculated as follows:

$$S(\lambda) = F \cdot \alpha(\lambda) \cdot P_0(\lambda). \tag{2.1}$$

Here, F specifies the properties of the applied environment (cell) and the excitation itself, $\alpha(\lambda)$ is the absorption coefficient of the gas dependent on the wavelength λ and $P_0(\lambda)$ is the optical power of the light source at the

given wavelength.
In general, the applied environment must be carefully selected. Most often, photoacoustic spectroscopy is employed in so called photoacoustic cells, which are introduced in the subsequent section. Corresponding to Haisch [17], the previously introduced cell constant F, for operating the photoacoustic cell in resonant mode, can be defined in the following way:

$$F = \frac{G \cdot (\gamma - 1) \cdot L}{\omega \cdot V} \cdot Q. \tag{2.2}$$

G is a geometrical correction factor, γ the specific heat, L and V are the length and the volume of the cell, ω the modulation angular-frequency and Q the quality factor of the cell.

2.1.2.2. Photoacoustic Cell Design

In PAS, photoacoustic cells are used to amplify the signal and to protect it against noise from the environment. By confining the acoustic wave through boundaries, it may increase significantly. This happens through constructive interference, which builds a standing wave.
Different types of acoustic resonators exist, e.q. cavity resonators, Helmholtz resonators or cylindrical resonators. In this work only the latter mentioned resonator type is further considered. An overview of PAS, including other types of resonators is given in [18].
In one dimensional cylindrical resonators, the acoustic wave propagates only in one direction, if the resonator diameter is much smaller than the length. A cylindrical resonator can be a simple tube with open or closed ends. In case of open-open or closed-closed ends, the resonance frequencies are integer multiples of the half wavelength and can be calculated as follows according to [18]:

$$f_n = \frac{n \cdot c}{2 \cdot (l + \Delta l)}. \tag{2.3}$$

According to Equation 2.3 f_n specifies the resonance frequencies, which occur at integer multiples of the fundamental resonance frequency, n is the

number of the desired resonance, c is the speed of sound, l is the length of the resonator (tube), and Δl is an end correction factor, which can be calculated with the aid of expression $\Delta l \cong 0.6r$ (r is the radius of the tube). When constructing photoacoustic cells, several criterias must be considered. The minimum cross section of the resonator is determined by the excitation source and the following collimation of the beam. The volume of the cell must be kept small and therefore, the cross section of the resonator tube has to be minimized, in accordance with Equation 2.2.
In general, resonators require protection from environmental noise by connecting them to volumes with much bigger cross sections, to induce acoustic reflections at the end of the tubes. This is mostly implemented through acoustic buffer volumes. A characterization of a photoacoustic detection, including the influence of the buffer volume size can be found in [19]. It is shown, that the photoacoustic signal increases with extended volume of the acoustic buffer.
Supplementary, different sources of noise have very strong impact on the sensitivity of the photoacoustic detector. The light beam through the cell induces noise through scattering light, which hits the resonator walls. In addition, window noise is generated, when the beam enters the photoacoustic cell. The induced gas flow through the cell is another noise source, which should be minimized. Another aspect is the selection of the modulation frequency. The photoacoustic signal S increases with descending modulation frequency (cf. eq. 2.2). Nevertheless, several noise sources have a $1/f$ frequency dependence (acoustic noise, electronic noise). As a consequence, it is recommended not to employ the modulation frequency below 1 kHz [18].
Different concepts exist to minimize the noise in the final photoacoustic signal. One possibility is to design a cell with two identical resonators, where the first resonator is excited through the modulated light source $S_{excited}$ and the second resonator is utilized to measure the noise $S_{background}$ (flow noise, background noise). The resulting photoacoustic signal is thereby calculated as follows:

$$S = S_{excited} - S_{background}. \tag{2.4}$$

Few papers used this configurations and reported a different outcome. Rück

et al. [19] did not report any improvements by the usage of a differential resonator, but did not exactly specify the cause. Yin et al. [20] and Zheng et al. [21] presented differential detectors, which improved the overall sensitivity of the sensor. Yin et al. [20] reported a minimum of detection down to the parts per trillion (ppt) level for NO_2 by the utilization of a high power laser. Zheng et al. [21] achieved a limit of detection of 3.6 ppm for methane, using an interband cascade light emitting diode (ICLED).
Generally speaking, theoretical calculations are necessary for the coarse design of the cell. For the final design, multi-physical simulation are highly recommended. This simulations can comprise the determination and tuning of the resonance characteristic, the distribution of the acoustic pressure and the assessment of the sound pressure amplitude.

2.1.2.3. Nitrogen Dioxide and Cross Sensitivity to other Pollutants

Subsequently to the introduction to PAS and the PA cell design, this section delves into the detection of nitrogen dioxide. NO_2 is a toxic, penetrating and pungent smelling gas, which is formed due to natural and anthropogenic processes, as successor of nitrogen oxide (NO) (see Figure 2.2). Automotive fuel combustion is the main anthropogenic source in Europe, although it is also generated due to other combustion procedures, like electric power generation through the burning of fossil fuels. Apart from that, natural sources include lightning or volcanic activities.

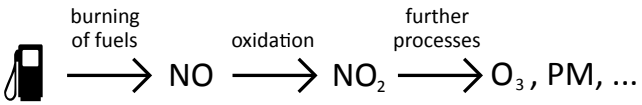

Figure 2.2.: Formation of nitrogen dioxide (NO_2) with precursor nitrogen oxide (NO) and reaction products of NO_2

Nitrogen dioxide is one of the key pollutants specified by the WHO [22] and the European Union (EU) [23], owing to the observed health risks. NO_2 causes diseases within the respiration chain of the body and it is a precursor for further pollutants like ozone or particulate matter, which supplementary

effect the human health.

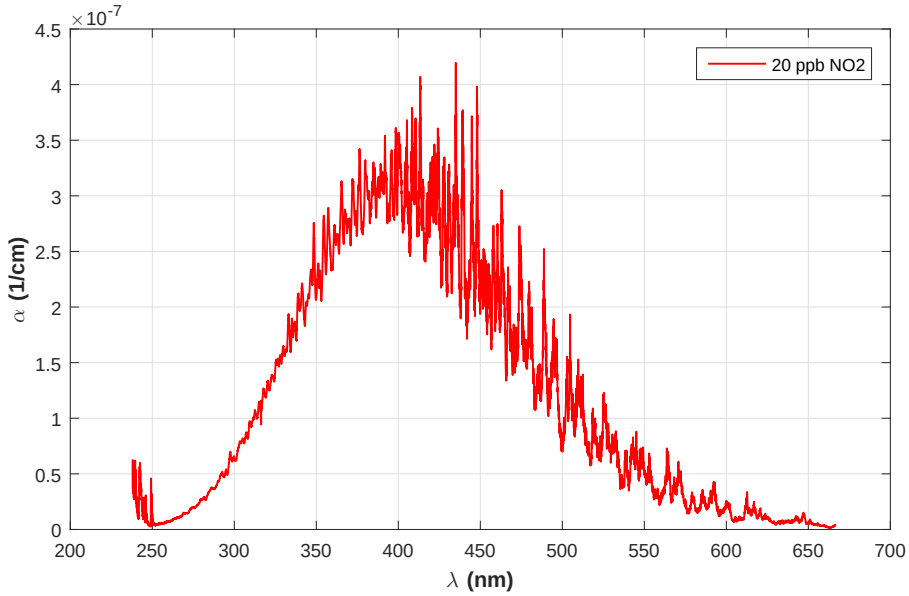

Figure 2.3.: Absorption spectrum of nitrogen dioxide (NO_2) in the visible light region [24].

By means of PAS, NO_2 can be detected considering the optical absorption spectrum of the gas. In Figure 2.3, the absorption spectrum for the visible light region of a nitrogen dioxide concentration of 20 ppb is illustrated. It can be seen, that the gas has its peak absorption around 400 nm. Due to the effect of photolysis (see Jones et al. [25]), which causes the decomposition of nitrogen dioxide into nitrogen oxide and oxygen, PAS should be applied above 430 nm for proper detection of the concentration.
The detection of one specific gas through PAS can be influenced by the cross sensitivity to other gases or particles. This depends on the absorption spectrum of the pollutants and has to be considered. Figure 2.4 shows the absorption spectra of ozone (O_3), sulfur dioxide (SO_2) and the USA model of air. Typical concentrations in the EU were selected for the illustration. The figure represents, that ozone or sulfur dioxide do not influence the absorption spectrum of NO_2. In contrary, the USA model for air shows several peaks above 400 nm, which should be avoided, when detecting nitrogen dioxide. Another important environmental gas, carbon monoxide

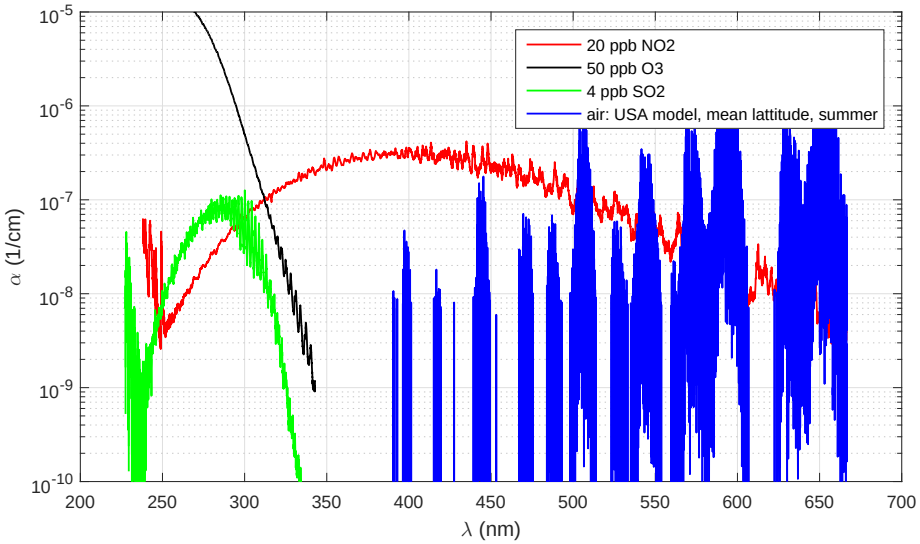

Figure 2.4.: Absorption spectrum of ozone (O_3), sulfur dioxide (SO_2), nitrogen dioxide (NO_2) and the USA model for air [24].

(CO), which is not shown in the figure, has its absorption peaks well above the visible light region ($\geq$1500 nm).
Of importance is the inclusion of soot in the consideration. Soot has a very widespread absorption spectrum and should be filtered, when detecting nitrogen dioxide or other gases. This can be done with appropriate particle filters.

2.1.2.4. Acoustic Measurement

Within PAS, the resulting acoustic wave requires a detection mechanism. Therefore, various properties have to be considered, dependent on the requirements. These properties encompass sensitivity, dynamic range, signal to noise ratio (SNR) or the construction form of the acoustic sensitive device. Common techniques to detect the acoustic pressure wave discussed in the literature are the usage of microphones, quartz tunings forks, or cantilevers. Quartz tuning forks (QTF) are the latest appeared method (cf. [13, 26]). Their usage as acoustic sensitive device is based on the piezoelectric effect, in

which charges are generated owing to deformation of the QTF. Usually transimpedance amplifiers are employed to enhance the signal to a detectable magnitude. In most application, the forks prongs are utilized to sense the acoustic signal in between. The resulting bending direction is consequently outward and therefore apart from each other. One supplementary benefit is, that they are not vulnerable to acoustic noise due to the same bending direction of the prongs. Quartz tuning forks protrude with their high quality factors and their mass manufacturing capabilities, but are susceptible to oscillations. A profound introduction to QTFs can be found in [27].
Micro electrical-mechanical system (MEMS) cantilevers are another possibility to sense acoustic signals. Similar to QTFs, they bring along very high quality factors, but are in contrast susceptible to acoustic noise. Acoustic signals can be measured by the displacement of the cantilever. Most often Michelson interferometers are utilized to measure the movement by evaluating the interference of a laser beam, which is reflected off the cantilever. They are often used in trace gas sensing. Kuusela et al. [14] measured several gases including carbon dioxide and sulfur dioxide in the ppm region, using a cantilever and an interferometer for detection. Fonson et al. [28] utilized a dual cantilever approach to enhance the sensitivity through the suppression of noise. An introduction into cantilever design and the usage in PAS gas sensing can be found in [29].
In general, the most common employed acoustic sensor devices are microphones. Different technologies exist, like electret condenser or MEMS microphones. Both mentioned technologies are based on the measurement of a capacitive change. Electret condenser microphones (ECM) employ a ferroelectric material as the static plate of the capacitor. Consequently, no bias voltage is required to keep the capacitive plate at a certain voltage level. The second plate is a moveable membrane, which is utilized to translate the acoustic pressure waves into variations in capacitance. The principle works as follows: an alteration in capacitance, caused by the moving membrane, leads to a voltage level change, which can further be enhanced by an electronic amplifier.
MEMS microphones apply a similar approach, only to be wrapped into a smaller package. Usually the static capacitive plate is not pre-charged. Rather than that, an internal charge pump is used to provide the fixed voltage level. These microphones are manufactured through standard complementary metal oxide semiconductor (CMOS) processes and are therefore

cheaper than ECMs. Within the package, an application specific integrated circuit (ASIC) is utilized to amplify the voltage change. Analog and digital versions exist, whereas the digital variants additionally integrate an analog to digital converter (ADC), to deliver the acoustic data through a data stream. Numerous publications employed different types of microphones in PAS gas sensing [10, 12, 21, 30, 31].
Supplementary, an extensive analysis of analog front end circuitries for microphone amplifiers can be found in [32].

2.1.2.5. Lock-In Amplification

Electronic signals and in particular PAS signals are often buried by noise or interfering signals with higher amplitudes, but different frequencies. These signals require special filtering or detection, to be properly retrieved from the background. Therefor several techniques, like very sharp bandpass filters, fast fourier transformation (FFT), goertzel algorithm or lock-in amplification (LIA) exist. The latter can be seen as a very sharp bandpass for filtering single frequency tones, if properly implemented. Lock-in amplifiers are often used within research laboratories or highly sophisticated measurement equipment for signal detection (cf. [12, 19, 21, 30]).
LIAs employ a reference signal for detection. The reference specifies the frequency of interest, which should be detected. In addition, the reference signal form is from particular significance, due to the including spectral components. If a single frequency tone should be detected, a pure sine wave is advantageous. Other possible signal shapes are rectangular, or triangular waveforms. They bring along the detection of harmonics of the fundamental wave.
A basic LIA structure is shown in Figure 2.5. In the primary (upper) path, the reference signal is multiplied with the signal of interest. Subsequently, the resulting signal is low-pass filtered. This step is of particularly importance, due to the nature of the previous multiplication, which is expressed through Equations 2.5 to 2.7.
In case the frequencies of the reference (ω_{ref}) and the signal of interest (ω_{sig}) are equal, the result includes a direct current (DC) term and a cosine term, dependent on twice the reference frequency. The second, frequency dependent term, must be removed to finally obtain a DC signal. This final

DC signal is proportional to the signal amplitude. Consequently, proper low-pass filtering is required to remove all alternating current (AC) components.

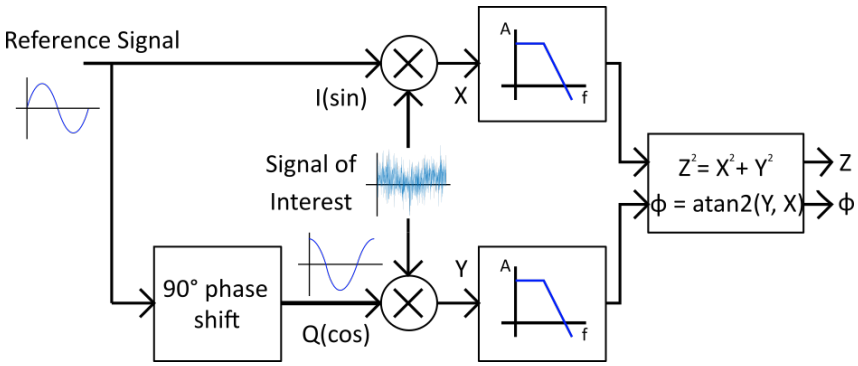

Figure 2.5.: Block chart of the lock-in amplifier theory. The reference signal is in the first path mixed with the signal of interest. In the second path, the reference signal is 90° phase shifted and afterwards mixed with the signal of interest. Thereafter, the resulting signals X,Y are low-pass filtered to remove all AC components. Finally the amplitude Z and the phase ϕ are calculated.

$$X = V_{ref}\, sin\left(t\omega_{ref} + \phi_{ref}\right) \cdot V_{sig}\, sin\left(t\omega_{sig} + \phi_{sig}\right) \tag{2.5}$$

$$= \frac{1}{2} V_{ref}\, V_{sig} \cdot cos\left(t\omega_{ref} + \phi_{ref} - \left(t\omega_{sig} + \phi_{sig}\right)\right) \cdot cos\left(t\omega_{ref} + \phi_{ref} + t\omega_{sig} + \phi_{sig}\right) \tag{2.6}$$

$$for\ \omega_{ref} = \omega_{sig} = \omega:$$

$$= \frac{1}{2} V_{ref}\, V_{sig} \cdot cos\left(\phi_{ref} - \phi_{sig}\right) \cdot cos\left(2t\omega + \phi_{ref} + \phi_{sig}\right) \tag{2.7}$$

Still, a phase dependency in the resulting signal exists. This phase dependency can be removed by additionally multiplying the signal of interest with a 90° phase shifted signal (see lower path of Figure 2.5) and consequently low-pass filtering the multiplication result. By the usage of the two Equations 2.8, 2.9, the amplitude Z and the phase ϕ can be calculated out of the two LIA signal paths.

$$Z = \sqrt{X^2 + Y^2} \tag{2.8}$$

$$\phi = atan2(Y, X) \tag{2.9}$$

Implementation-wise different capabilities exist to implement LIAs. Firstly, they can be implemented in an analog form using mixer and low-pass filter circuits. Secondly, they can be realized fully digital by sampling the signal of interest and calculating the reference signal via the processing unit. Thirdly, in a hybrid approach. Fully analog implementations bring along non-linearity effects and reliance on temperature variations. Within digital implementations, the processing power and possible large data storage requirements are indispensable, if the calculations are not done online.
A detailed introduction into lock-in amplifier theory can be found in [33].

2.2. Sensor Network

The sensor network theory is skipped in this part of the work, but an introduction can be found in the attached paper A, which was composed during this work.

3. Methodology

This chapter gives an insight of how the sensor system is designed and of which parts it consists. Primarily the entire sensor system is illustrated in block level view, to represent the chosen concept. Thereafter, the individual blocks are presented in more detail.

3.1. System Design

The sensor system consists of five major blocks depicted in Figure 3.1. The physical basis and therefore the foundation of the sensor, is the photoacoustic cell. The cell is used to enhance the photoacoustic signal through the utilization of resonators and further protects against noise and disturbances from the environment. It is therefor composed out of two resonators, which are connected on both ends to acoustic buffer volumes. A microphone is mounted in the middle of each resonator, to measure the acoustic wave. Gas openings are placed at the top of the buffers, to measure the gas of interest. The collimation of the incoming LED beam is realized with a convex lens, which is mounted at the entrance of the cell. Additionally, to reflect the LED beam back into the resonator, a concave mirror is placed at the end of the photoacoustic cell. The reflection results into an enhanced beam intensity in the resonator.
The second principal block is composed out of the signal generation circuit and the previously mentioned LED. The signal generation is built around a voltage controlled oscillator (VCO), which generates a square wave with adjustable frequency. Using this signal, a sine and a cosine waveform are generated through dedicated circuits. On the one hand this provides the modulation source for the LED and on the other hand it is used as reference input for the digital lock-in amplifier.

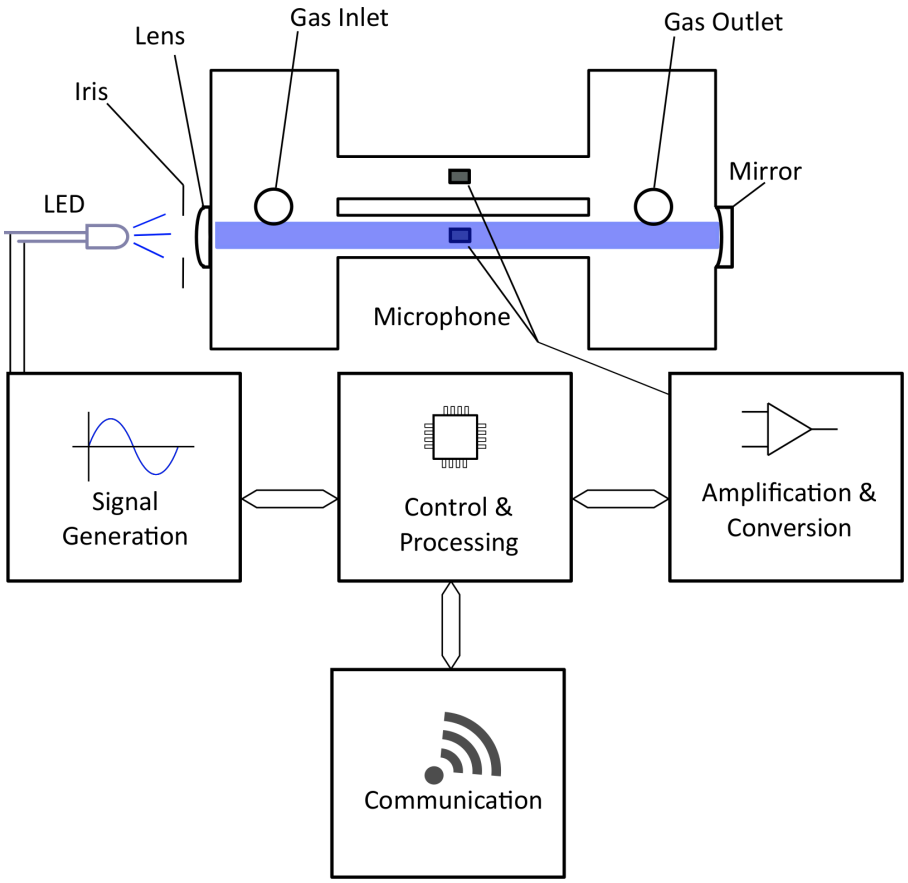

Figure 3.1.: Block level diagram of the sensor system design. The system consists out of 1) a resonant cell, 2) a signal generation circuit which controls the LED, 3) two microphones to measure the acoustical signals which are connected to a amplification and digital conversion circuit, 4) the LoRa transceiver for data transfer and 5) the central control and processing unit.

In addition, to quantify the acoustic wave generated by the excited gas through the modulated LED beam, two microphones are employed in the third fundamental part of the system. One microphone is utilized to translate the acoustic wave into an electric signal, whereby the second microphone is used to measure the background noise. The resulting microphone signals are thereafter fed into an analog amplification stage and are then converted into the digital domain, to be processed.
The fourth major element in the system features the control and processing

capabilities. Therefor, an ultra low power STM L476RG ARM based microcontroller was chosen. The controller is responsible to fetch the converted microphone signals, to control the signal generation circuit, to further process the obtained data by the lock-in technique and to transfer the data to the LoRa (integrated circuit) IC.
Finally, the fifth major part in the system is the sensor network component, which is a SX1272 transceiver with LoRa capability. This transceiver stands out by low power consumption and long communication range, which is qualified for distributing the resulting sensor data.

3.2. Optics

As previously introduced, a LED is utilized as photoacoustic excitation source for the gas inside the cell. In the next two sections the selection of the LED is described, as well as how the divergent LED beam is collimated.

3.2.1. LED as Excitation Source

For this sensor setup a LED was selected, based on the matter of price and the simplicity of the electronic driver. The requirements for the LED were:

- The peak wavelength must fit to the absorption spectrum of NO_2 (see Figure 2.3),
- maximum optical output power with the lowest possible power consumption, and
- the radiation angle (half viewing angle) has to be as small as possible for proper collimation.

As a consequence, the LED450-06 from the LED450-series from Roithner LaserTechnik GmbH was selected. This LED has an optical output power of 20 mW, when driven with 20 mA. This results in a reasonable efficiency compared to other LEDs. In addition, the half viewing angle of $\pm 4^\circ$ is very small compared to conventional LEDs and thus, the losses owing to collimation are reasonable.

Figure 3.2 shows the radiation spectrum of the LED in contrast to the absorption spectrum of NO_2. The peak wavelength is specified at 450 nm, which does fit well into the absorption cross section of NO_2. A LED with differing peak wavelength from the maximum absorption section of nitrogen dioxide was selected, due to the effect of photolysis (cf. Section 2.1.2.3).

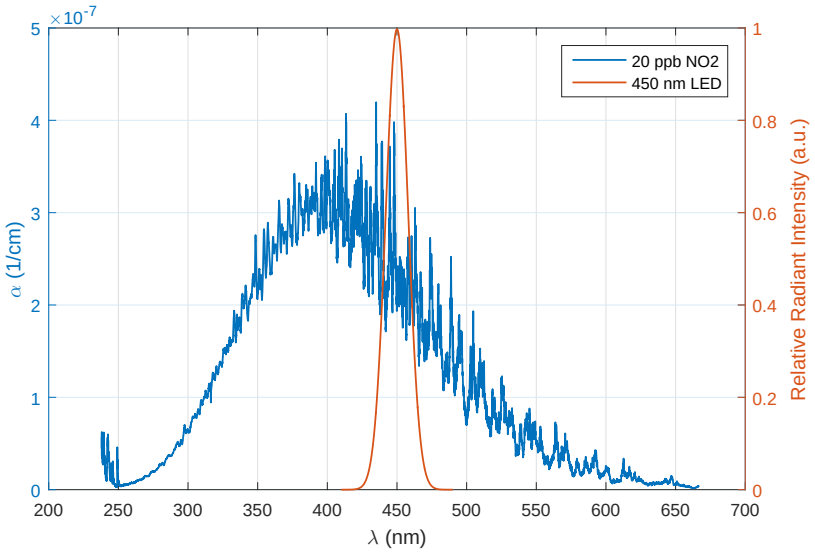

Figure 3.2.: Absorption spectrum of NO_2 in the visible light region compared to the radiation spectrum of the chosen LED (LED450-06).

3.2.2. Collimation of the Divergent LED Beam

In contrast to most lasers, LED beams are highly divergent and therefore difficult to collimate. Hence, the beam can only be collimated or confined across a certain distance. Due to the resonator structure, which is described in Section 3.4, the requirements were less stringent. This resulted into the restriction, that the beam diameter should not exceed the resonator cross section of 10 mm, mainly due to the generation of noise.
On this account, the best fit was a plano-convex lens, to be utilized for collimation at the entrance of the cell (cf. Figure 3.3). A Thorlabs LA1422-A-N-BK7 plano-convex lens was selected, with a focal distance of 40 mm.

In front of the lens an aperture is placed to limit the angle of incidence. In addition, to reflect the LED beam back into the resonator and therefore, to enhance the photoacoustic signal, a concave mirror is mounted at the end of the second buffer volume. This was utilized with a Thorlabs CM254-075-P01 silver-coated concave mirror (focal distance of 75 mm). Using this mirror the photoacoustic signal can be enhanced by approximately 50 percent. The complete optical setup is depicted in Figure 3.3.
In general, an optical multistage setup can most certainly provide a better collimation of the beam. However in this case, the single stage setup is sufficient.

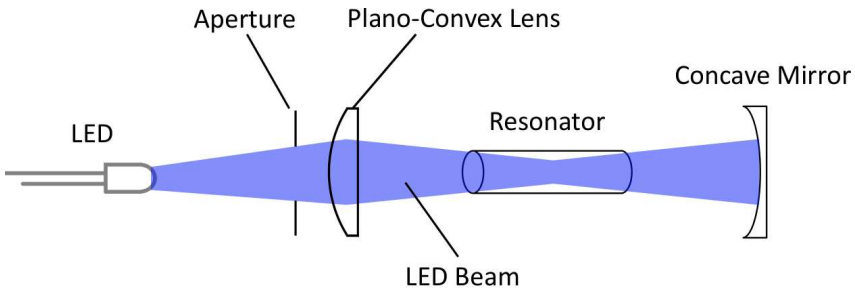

Figure 3.3.: Schematic representation of the collimation of the divergent LED beam. The collimation is utilized with a plano-convex lens. In front of the lens is an aperture placed to stop the most divergent rays. On the other end of the cell a mirror is mounted, to reflect the beam back into the resonator.

3.3. Acoustic Detection

According to the photoacoustic effect (Section 2.1.2.1), a conversion of the sound pressure level (SPL) to an electric equivalent is required for further processing. For this work, a Knowles EK23029 electret condenser microphone was chosen owing to several criteria. First, the EK23029 has a cylindrical entrance port, which is qualified for proper mounting in a resonator tube. Second, the microphone has a higher sensitivity compared to standard MEMS microphones, with a minimum value of less than -30 dB/Pa. The corresponding sensitivity curve is shown in Figure 3.4.
Considering the sensitivity characteristic, another advantage of this microphone is the suppression of low frequency noise.

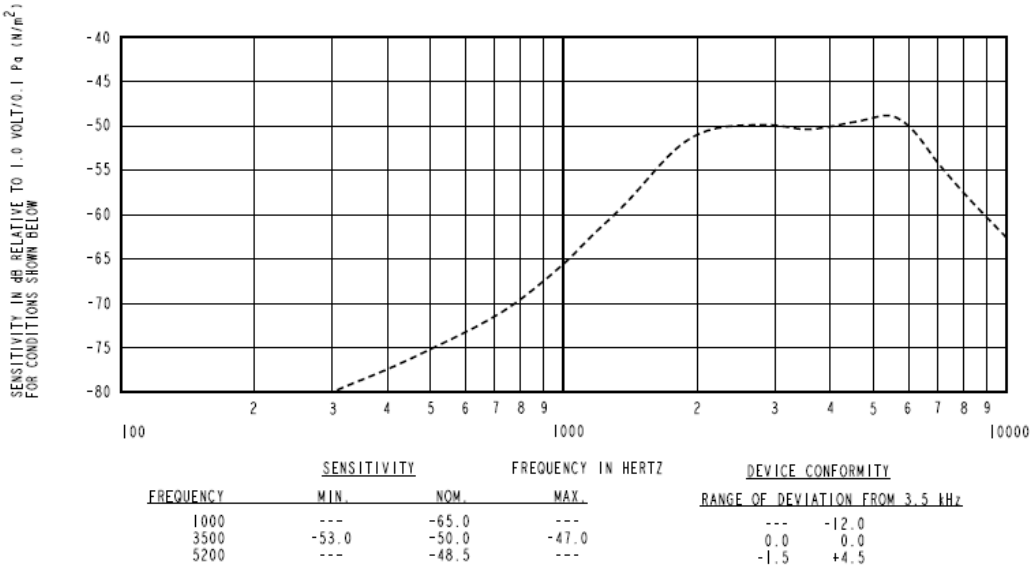

Figure 3.4.: Sensitivity and device conformity of the Knowles EK23029 electret microphone [34].

3.4. Photoacoustic Cell Design

In the following part of the work the photoacoustic cell design is described. The photoacoustic cell is the fundamental physical basis of the sensor. Previously, in Section 2.1.2.2, the theoretical basics were given. Subsequently, the simulation of the cell using Comsol Multiphysics 5.3a is depicted and afterwards the cell construction is presented.

3.4.1. Simulation

Prior to the simulation, the potential resonance frequency range was defined, by the utilization of the EK23029 microphone. Owing to the microphones sensitivity characteristic, the range from 2 kHz to 6 kHz should be used (cf. Figure 3.4). Therefore, the resonance frequency was chosen to be $f_n = 2200Hz$. With the usage of Equation 2.3, the following approximate value of

the resonator length was calculated:

$$l = \frac{n \cdot c}{2 \cdot f_n} - \Delta l = \frac{n \cdot c}{2 \cdot f_n} - 0.6 \cdot r = \frac{1 \cdot 343.2 \frac{m}{s}}{2 \cdot 2200 Hz} - 0.6 \cdot 0.01 m = 0.072 m. \quad (3.1)$$

Within Equation 3.1 n was set to 1 for a $\frac{\lambda}{2}$ acoustic wave, the sonic speed c is 343.2 $\frac{m}{s}$ at 20°C, the resonance frequency was set to 2200 Hz and the diameter of the resonator tube r was defined with 0.01 m.
As a second step the resonator type was selected. It was decided to design a differential cell for background noise cancellation, where two resonators with the same dimensions are used. In the first, active resonator, the gas is excited through the incoming light. The second resonator is utilized to quantify the background signal (gas flow noise, window noise, background noise). In addition, two volumes, one on each side of the resonators, are placed as acoustic buffers. To accomplish a simulation as accurate as possible, the microphone ports in the middle of the resonators and the recesses for the lens and mirror mounts are additionally included.
Mainly, the following two objectives were defined to dimension the photoacoustic cell: 1. maximization of the acoustic signal and 2. preferable sparse interaction between the two resonators. For the optimization, the following parameters were varied:

- radius and length of the buffer volume,
- radius of the resonator tubes, and
- distance between the resonator tubes.

As a result, the following insights were observed:
1) According to expectations (cf. Miklòs et al. [18]), the radius of the resonator tube is inversely proportional to the amplitude of the acoustic wave.
2) The volume of the acoustic buffer is proportional to the amplitude of the acoustic wave and inversely proportional to the resonant frequency of the cell, which was also discovered by Rück et al. [19].
3) From the simulation emerged, that the length and radius of the buffer volume have an impact on the acoustic wave. This happens because the minimum pressure node is locally shifted according to the dimensions. As a consequence, the location of the two resonator tubes is affected.
4) The coupling between the resonator tubes is proportional to the distance

between them. This applies up to a detachment of a half wavelength. On the contrary, the irradiation of the light beam into the passive resonator tube increases with decreasing distance.
Overall, the simulation resulted in a very strong coupling between the two tubes (cf. Figure 3.5), although the heat source was only applied through the active resonator. On that account, the cell was additionally simulated without the second, passive resonator (cf. Figure 3.6). The objective for this simulation was to have a maximum amplitude at the microphone slot of the active resonator and a minimum sound pressure level (SPL) at the entrance of the second tube.

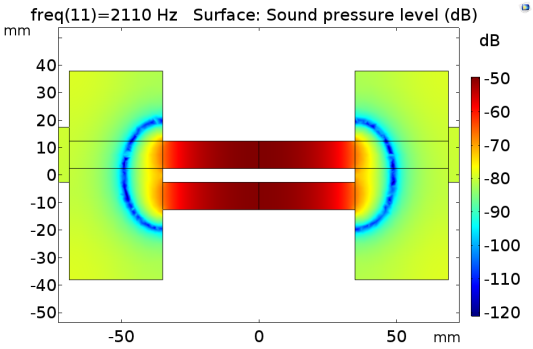

Figure 3.5.: Cross section of the thermoviscous simulation of the photoacoustic cell with both resonator tubes.

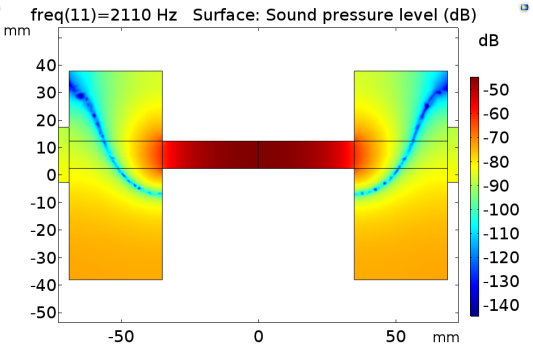

Figure 3.6.: Cross section of the thermoviscous simulation of the photoacoustic cell with a single resonator tube.

Consequently, the cross section of the final cell dimensions at the used eigenfrequency is depicted in Figure 3.5, where the SPL distribution is shown. Figure 3.6 shows the simulated cell without the second resonator tube. It can be observed, that at the center of the active resonator tube a pressure maximum occurs and at the entrance of the second (not shown) tube a pressure minimum is formed.
Additionally, the SPLs at the microphone slots for a frequency-sweep around resonance are plotted. The plots are shown in Figure 3.8 for the final photoacoustic cell with two resonators and in Figure 3.7 without the passive resonator. It is apparent, that in both plots, the difference between the two curves enlarges with increasing distance from the resonance frequency.

In Table 3.1, the final dimensions of the PA cell are represented. The res-

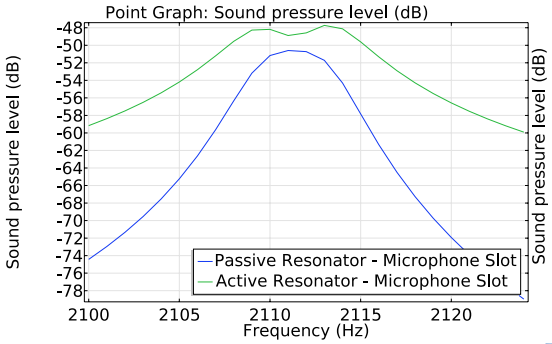

Figure 3.7.: Frequency sweep of the acoustic simulation with both resonator tubes.

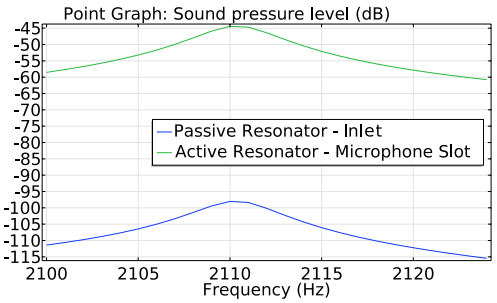

Figure 3.8.: Frequency sweep of the acoustic simulation with single resonator tube.

onator radius is constrained by the diameter of the LED beam and was set to a minimum value of 10 mm. The distance between the resonator tubes was optimized for minimum coupling and therefore defined to 15 mm.

Name	Value
Resonator Length R_{len}	70 mm
Resonator Radius R_r	10 mm
Resonator Distance R_{dist}	15 mm
Buffer Length B_{len}	34 mm
Buffer Radius B_r	38 mm

Table 3.1.: Final photoacoustic cell dimensions. The resonator distance is the length between the center of both tubes.

Contemplating the observed dependencies of the buffer dimensions, the length was set to approximately $\frac{\lambda}{4}$. The radius of the buffer volume was determined to 38 mm.

3.4.2. Cell Construction

Following the determination of the cell dimensions, the design of the cell construction is described in this part of the work. In Figure 3.9, the schematic

drawing of the photoacoustic cell is shown. It was decided to build the cell by the utilization of a hybrid approach. The buffer volumes of the cell are 3D printed using a Formlabs Form 2 printer. In contrast, the resonators were cut from stainless steal tubes, whereby the equality of both tubes is from vast significance. The resonator tubes were not printed, due to self heating and insufficient reflection of the photopolymer material caused by the divergent LED beam. The sealing of the cell and the attached components, in particular connections to the resonator tubes is from high importance. Accordingly, the tubes were bonded to the buffer volumes and the microphone inlets by the usage of silicon glue.
In Figure 3.10 the cross section and in Figure 3.11 a 3D view, of the constructed PA cell are depicted.

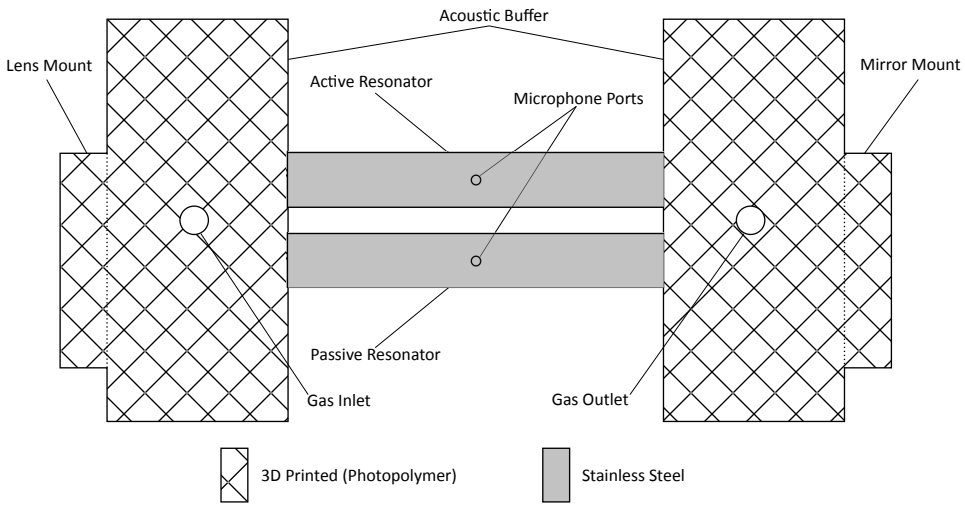

Figure 3.9.: Schematic drawing of the cross section of the photoacoustic cell.

To attach the microphones to the resonator tubes a bracket with four mounting holes was inserted into the construction. By the utilization of these holes microphone printed circuit boards (PCB) can directly be attached to the cell. In addition, recesses for mounting the lens and mirror holder are included in the cell design.

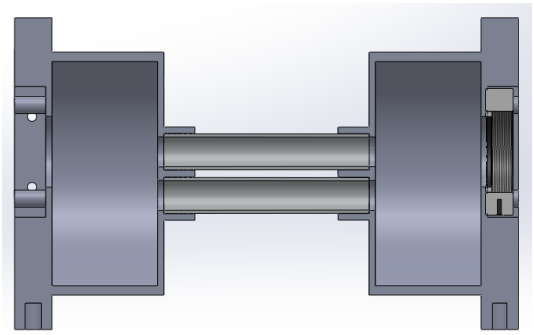

Figure 3.10.: Cross section of the photoacoustic cell construction.

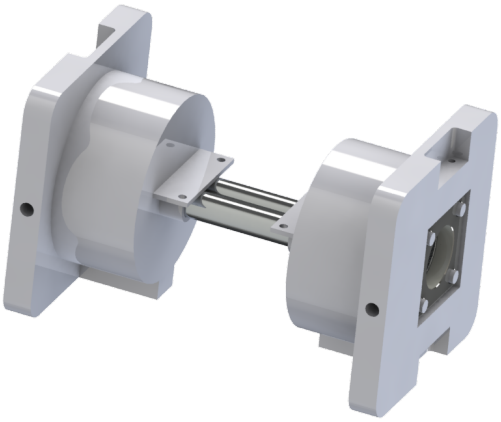

Figure 3.11.: 3D view of the constructed photoacoustic cell. Gas inlet and outlet are not shown.

3.5. Signal Generation

Subsequent to optic collimation and cell design, the signal generation for the excitation source and consequent lock-in detection is discussed in the following. The main prerequisite is the frequency resolution of the modulated signal, since frequency sweeps are required to detect the resonance frequency. This is expected due to variations of the resulting cell dimensions, compared to the utilized values in pre-calculations and simulations. In addition, environmental conditions, like humidity or temperature variations, are presumed to have an influence on the resonance frequency.
According to this, a minimum resolution of 1 Hz is defined as requirement. Further, due to the chosen detection method (described in Section 2.1.2.5) two waveforms are required. First the exciting signal and second the quadrature component, which is a 90° phase shifted waveform compared to the exciting signal. These signals should contain only a single frequency component, since impure signals degrade the sharp bandpass characteristic of the LIA. Several prospects exist to generate the signals, including direct digital synthesis (DDS), pulse width modulation (PWM) or the usage of oscillators. The utilization of DDS integrated circuits (IC) is a straightforward variant, since they are easy to use and often implement frequency sweep function-

ality. In the case of low power design, the main disadvantage is, that most parts have a vast power consumption. In addition, they produce impure waveforms because of their output digital to analog converters (DAC). As a consequence, it was decided to develop a dedicated circuit for the signal generation.
The block level schematic of the signal generation circuit is shown in Figure 3.12. A VCO (LTC6990) was chosen as basic frequency-dependent signal generation device.

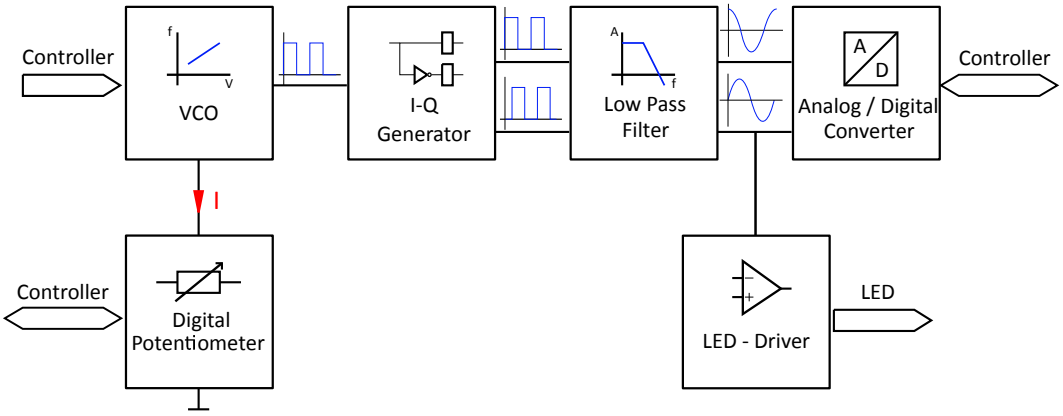

Figure 3.12.: Schematic drawing of the signal generation circuit.

The frequency of the device can be programmed by the utilization of a single resistor. A fixed resistor R_{fixed} is employed to set the approximate frequency range. Additionally, to be able to variate the frequency in this range, a 12 bit digital potentiometer R_{pot} is utilized. With this compound a frequency range of about 550 Hz, with a resolution of less than 0.5 Hz, can be achieved. Equation 3.2 defines the calculation of the VCO frequency, where N_{div} is defined by a fixed voltage divider.

$$f_{out} = \frac{1MHz}{N_{div}} \cdot \frac{50k\Omega}{R_{fixed} + R_{pot}} \tag{3.2}$$

At the output of the VCO, a rectangular I-Q generation circuit is deployed, to generate a rectangular signal and a 90° phase shifted rectangular signal. This circuit can be obtained with two D-Flip-Flops and an inverter, as described in [35]. Thereafter, the two rectangular signals are filtered at the

output of the I-Q generator, using two low power 8th order progressive elliptic low-pass filters (LTC1069-1). The cutoff frequency of the filter is set to 2.5 kHz. With the utilization of these filters, a sine and a cosine wave are generated out of the initial rectangular waveforms, by suppressing the harmonics of the fundamental frequency. The two signals are subsequently converted to the digital domain, with the aid of a dual channel analog to digital converter (ADC). In addition, the sine wave is used as a possible input source of the LED driver circuit.

3.6. Signal Amplification and Conversion

This part of the work presents the amplification and conversion of the microphone signals. As previously explained, the first microphone is used to measure the acoustic signal generated by the excited gas. The second microphone is utilized to quantify and subtract the background noise, to enhance the accuracy of the sensor. Subsequently, an analog single channel and a mixed signal dual channel solution are described, to amplify and digitize the measured signals.

3.6.1. Solution 1: Analog Single Channel

The first concept processes the two microphone signals in an analog manner. Figure 3.13 shows a schematic illustration of the circuit. An instrumentation amplifier was chosen to subtract the signals to remove the background noise. Prior to the subtraction, the analog microphone signals are filtered through a simple band pass filter. This filter is implemented by a basic RC structure.

Thereafter, the filtered signals are firstly amplified and subsequently subtracted by an instrumentation amplifier. The chosen amplifier, a AD8421, was selected by means of low noise $(3\frac{nV}{\sqrt{Hz}}, 200\frac{fA}{\sqrt{Hz}})$, low power (2.3 mA), high gain (up to 10000) and proper gain bandwidth product (GBP) characteristics. The gain is adjustable by an external resistor, whereby a gain of 60 dB is set. Following the instrumentation amplifier, the signal is converted

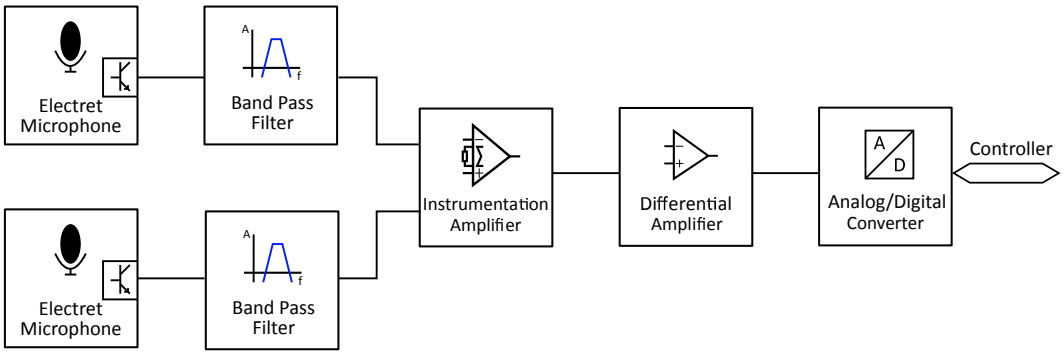

Figure 3.13.: First version of the signal amplification and conversion circuit. The analog microphone signals are subtracted with the aid of an instrumentation amplifier.

to the digital domain, with the aid of an 18-bit successive approximation register (SAR) ADC. To utilize the full strength of the converter, the single ended signal is converted prior to the ADC into a differential signal, by the usage of a fully differential amplifier (LTC1992-10).
The circuit was dimensioned with the aid of a simulation program with integrated circuit emphasis (SPICE) tool. The frequency response of the filter and amplification block is shown in Figure 3.14. The upper plot represents the magnitude response and the lower plot the phase response of the design. The target is to preferably suppress all spectral components besides the modulation frequency of 2200 Hz.

3.6.2. Solution 2: Mixed Signal Dual Channel

The second concept is a mixed-signal analog to digital solution, represented in Figure 3.15. In this design, the microphone signals are treated separately. After the internal amplifier of the microphones, the signals are bandpass filtered, similarly compared to the analog concept. Subsequently, an amplification stage with a gain of 30 dB follows. In this gain stage, a low power, low noise $(5.9\frac{nV}{\sqrt{Hz}}, 0.6\frac{pA}{\sqrt{Hz}})$, rail to rail amplifier (ADA4805) is employed, by the usage of a single IC (two amplifiers in one package) for both signal paths. The amplified signals are subsequently digitized through a special purpose analog front end (AFE). This IC, a MCP3911, comprises two synchronous

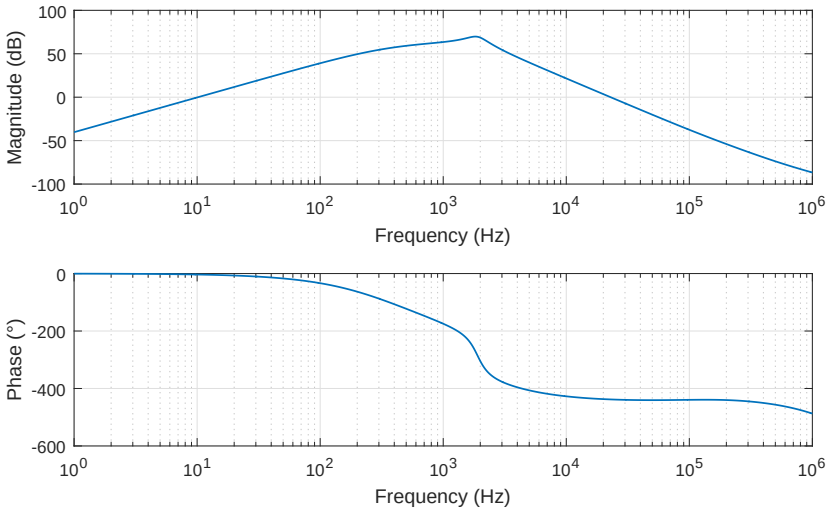

Figure 3.14.: Frequency response of the signal amplification and conversion circuit V1. The upper plot depicts the magnitude response, the lower plot shows the phase response.

sampling 24-bit ADCs, which are able to sample two signals in parallel.

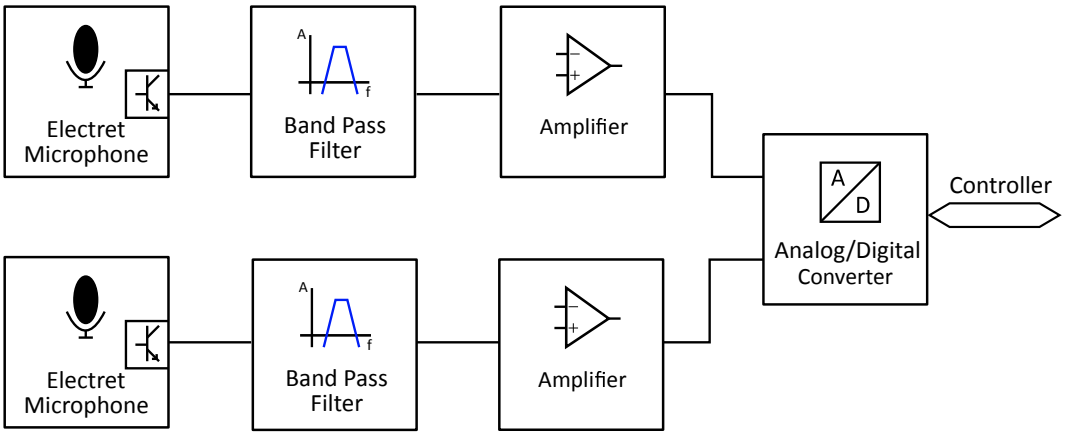

Figure 3.15.: Second concept of the signal amplification and conversion circuit. The microphone signals are separately amplified and converted to the digital domain.

Figure 3.16 shows the internal structure of the utilized AFE. The input stage of the MCP3911 consists of two programmable gain amplifiers (PGA), with

a maximum gain of 30 dB. Consequently, the amplified signals are fed into the ADC architecture, which is a sigma delta modulator. This type of ADCs are oversampling converters, comprising an integrator, a quantizer and a DAC.

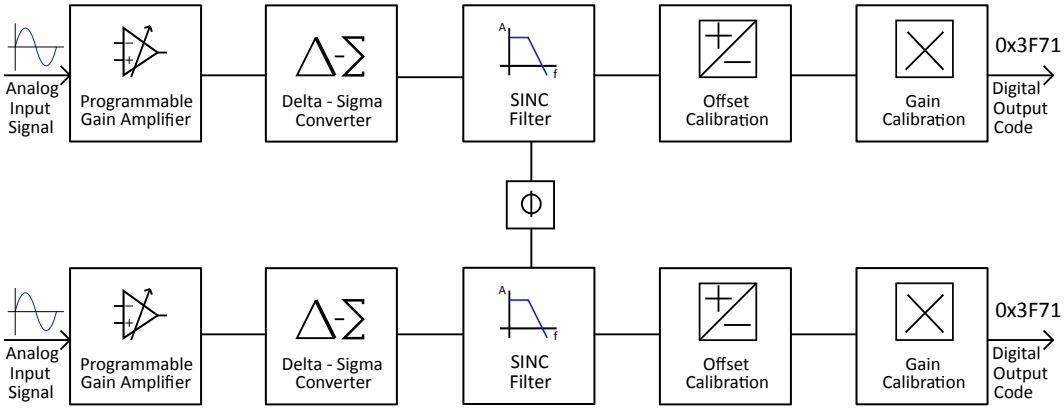

Figure 3.16.: Internal structure of the two channel Sigma-Delta ADC MCP3911 (cf. datasheet [36]). The ADC contains a phase compensation block, which is capable of changing the phase shift between the two channels. Additionally, the ADC comprises an offset and a gain calibration block per channel.

Following to the quantization, the bitstream is passed through a SINC filter, which contains a phase shift block. With the utilization of this block, the phase relation between the two AFE channels can be changed. This is a very beneficial feature, if the sampled signals contain a phase shift compared to each other, which can occur through mismatching in prior amplification or filter stages. The minimum adjustable phase shift depends on the sampling frequency of the ADC. With a sampling rate of 4 MHz, a time shift of 0.25 μs can be achieved. Translated to a phase for a signal-frequency of 2200 Hz, a minimum phase shift step of 0.2° can be achieved. Supplementary, the AFE is capable of adjusting the offset and the gain of both channels individually. The described settings (phase relation, offset and gain) can be set via the serial peripheral interface (SPI) of the AFE, which is connected to the controller.

3.7. Lock-In Amplifier Implementation

In PAS a signal detection mechanism is required, to filter the signal of interest from the background. In this sensor design a lock-in amplifier is realized, to implement the required signal detection. The theory covering the basics for this section, are described in the previous chapter (see 2.1.2.5). Conceptionally considered, a mixed analog and digital approach was chosen to implement the LIA. Figure 3.17 illustrates the concept.

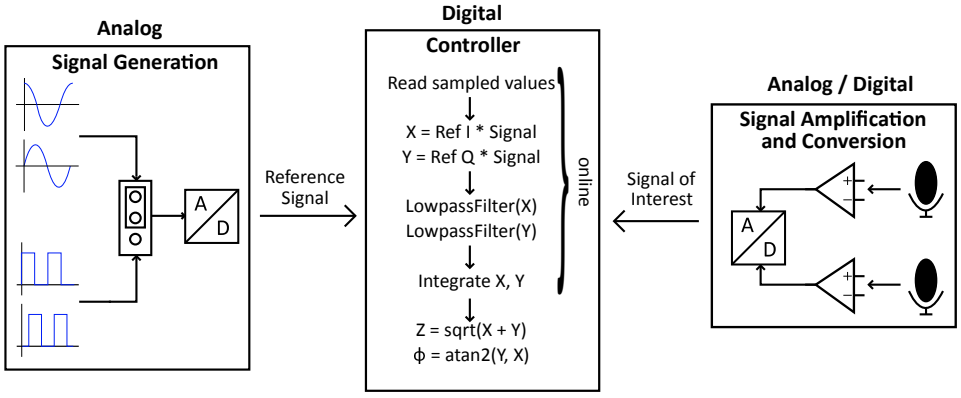

Figure 3.17.: Block diagram of the lock-in amplifier implementation. The reference signal generation part is mainly realized in an analog manner . Final calculations including mixing (multiplications) and low-pass filtering, are implemented digitally.

The reference signals are generated through a dedicated analog circuit, which is described in Section 3.5. The frequency of the reference is adjustable through the controlling unit via a SPI interface. The waveform of the reference signal is selectable through a jumper and can be chosen between sine and rectangular. Consequently, the signals are sampled through an on-board ADC to provide the waveforms to the controller.
Of main interest is the PA signal, which is measured, amplified and converted through the circuits described in Section 3.6. This is mainly done in an analog manner, although digital filtering and digital signal processing are applied through the AFE described in 3.6.2.
The basic LIA operations are realized digitally. A processor is utilized to implement this operations, which is described in more detail in the subsequent

section. Through memory capacity considerations, the signal multiplications and post low-pass filter is implemented online. Meaning, that during one sampling or calculation cycle, data is fetched from the ADCs, the signal of interest is multiplied by the reference signals and prior to the integration a moving average low-pass filter is applied. This is done for a period of time, dependent on the adjustable integration time of the LIA. Once the integration time is reached, the final lock-in results are calculated. The default moving average filter order is set to 200. It has to be mentioned here, that the performed online calculations have to fit into the sampling period. Otherwise, if the calculations would not fit into the sampling period, faulty results or unexpected behavior might occur.

3.8. Controller

Centrally, to control all parts of a system, a central processing unit (CPU) is often required. The CPU in this design is required to control the signal generation circuit, to control and retrieve the data sampled by the amplification and conversion circuit, to process the data afterwards and furthermore to handle the later described LoRa transceiver for the wireless data transfer. These demands require the following attributes:

- reasonable clock frequency to be able to perform the mentioned tasks,
- an SPI block to control the attached devices and to handle the data transfer. Thereby is a minimum SPI clock rate of 5 MHz required,
- preferably an internal floating point unit (FPU) to be able to perform the LIA calculations in time,
- low power consumption.

Taken this attributes to account, an ultra-low-power ARM based 32-bit STM32L476RG processor with internal FPU was selected as CPU. This processor can be clocked up to 80 MHz and has 4 SPI blocks, which are capable of data transfers up to 20 MHz. The STM32L476RG requires only 100 μA/MHz in run mode and 30 nA in shutdown mode. As prototype platform, a STM32 Nucleo board from ST Microelectronic is utilized. The Nucleo boards are prototyping platforms, which additionally to the microcontroller integrate an on-board debugger and feature several pin headers,

for supplementary daughter board or cable connection to the microcontroller ports.
In the following, it is described how the microcontroller is programmed and how the program is structured.

3.8.1. Real Time Operating System

The programming of microcontrollers encompasses mainly two different models. Historically, primary bare metal programming is used. This is in principal the more efficient programming model, without much overhead in case of program code, timing or memory usage. On the contrary, the programming effort is most often much higher, compared to the utilization of real time operating systems (RTOS), since many functionalities must be implemented. By contrast, the utilization of RTOS bring along the benefit of fast prototyping, support of different libraries or the abstraction from the hardware. Opposed to this, they are usually not as efficient as bare metal programs. In this application it was decided to use an operating system, because the prototyping and portability outweighs the required efficiency.
A vast amount of real time operating systems exist, which distinguish on several criterias like source model, platform or use case. In this work, mbed OS was selected to be an appropriate choice owing to several features. First, mbed OS supports the usage of LoRa. Second, the software is portable to all Cortex M cores and therefore, it is customizable in case of hardware. One drawback is the implementation of the timer and interrupt handling, which has a very raw time resolution (1 μs) up to this point.
Figure 3.18 shows a coarse structure of the used RTOS. Mbed OS builds upon the hardware specific implementation of the silicon vendors. In this case on top of the hardware abstraction layer (HAL) of ST Microelectronics for the STM32L476RG core. For the ARM Cortex M family processors, a Cortex Microcontroller Software Interface Standard (CMSIS) was introduced in 2008 by ARM to enable device portability. CMSIS defines the software interface, which the low level HAL of the vendors must provide. The core of mbed OS builds on CMSIS RTOS and includes functionalities like multi-threading support, a FAT file system or network support (TCP, UDP). In addition, it is possible to customize the components to reduce the system overhead. Upon

the basic operating system and the CMSIS standardized HAL, the drivers are implemented to provide the required peripheral functionality. On top of the RTOS runs the application code and further implemented shared libraries, like the SX1272Lib for LoRa usage.

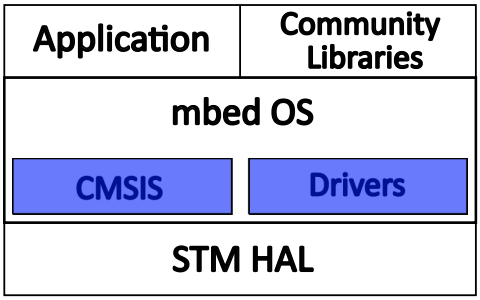

Figure 3.18.: Coarse software stack with the utilization of mbed.

3.8.2. Program Structure

In the following part, the application code of the sensor system is described. The application code runs on top of the operating system and provides the whole functionality to deal with the hardware, which was described in Section 3.5 and 3.6. A scheme of the application is depicted in Figure 3.19. The main program comprises the high level program flow, which starts with the initialization of the components. Thereafter, with the utilization of the mixed-signal amplification and conversion circuit, the ADC channels are calibrated concerning offset, gain and phase alignment. The resonance profile of the PA cell is subsequently characterized, to get the maximum signal amplitude for the following measurement. In real world applications, the calibration of the hardware and the characterization of the cell only needs to be done partly, depended on environmental factors like temperature or humidity.

To provide the methods for control and data retrieval of the hardware, the sensing functionality block implements on the one hand a class, which deals with the control of the VOC and therefore the signal generation. On the other hand, the sampling control for the data transfer of the used ADCs and the calibration mechanism is included in this block.

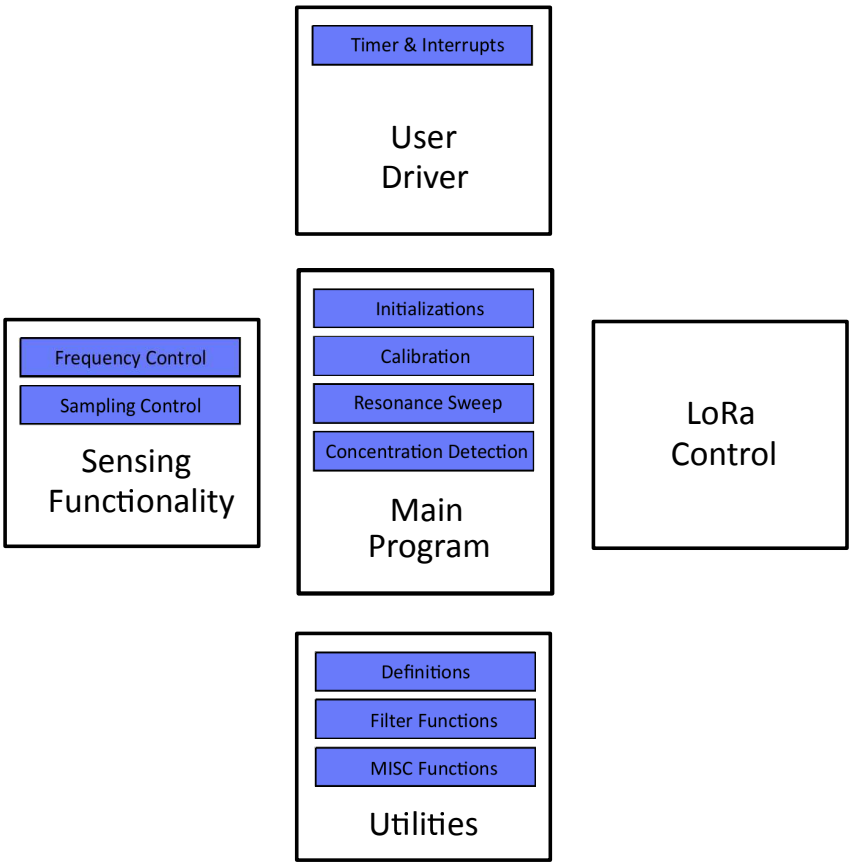

Figure 3.19.: Structure of the application program.

As already mentioned above, the implementation of the timer and interrupt handling, was done separately from the operating system. This is due to the fact that the time resolution of the mbed OS implemented timers is only 1 μs, whereby with a system clock of 80 MHz a time resolution of 12.5 ns is achievable. In case of the sampling system, where data is read from 4 ADCs with a frequency of about 16 kHz (every 62.5 μs), timer and interrupt handling are critical components.
The wireless data transfer capability is achieved by the utilization of an mbed library called SX1272Lib. This library features the full functionality for setting up the LoRa data transfer with the usage of a SX1272 LoRa transceiver, by providing methods for initialization, receiving and trans-

mitting. Therefore, only the logic for sending and receiving packets is additionally required.
Finally, the remaining methods are combined in the utilities block. This classes include filter functions for data processing or additional methods, which are used in the calculations or calibration procedures.
In general, the application is programmed in a modifiable manner, were most functionality can be altered, with the usage of defined constants.

3.8.2.1. Microphone Channel Calibration

With the utilization of the developed mixed signal dual channel hardware, for the microphone signal processing (cf. Section 3.6.2), it is firstly possible to sample the two signals individually. Secondly, the used AFE contains the feature of modifying the phase relationship between the two sampled signals. Supplementary, the MCP3911 contains two blocks per channel to modify the voltage offset and the gain. To take advantage of these features, three subroutines were developed to perform offset calibration, gain calibration and a phase adjustment between the channels. By performing these calibrations, the microphones, respectively the AFE channels, can be matched to each other. In this scenario the calibration routines are executed in the following order:

1. offset calibration,
2. gain calibration, and
3. phase adjustment.

Figure 3.20 depicts the sequential procedure of the offset calibration. In principle, during the offset calibration both microphone channels are sampled individually and the averaged offset value per channel Off_{CHx} is calculated by the utilization of Equation 3.3:

$$OFF_{CHx} = \frac{1}{N} \cdot \sum V_{CHx}. \tag{3.3}$$

Here, N specifies the number of samples and V_{CHx} is the sampled voltage level of the individual channel. Subsequently, circular buffers are used to

store the latest offset values and the difference between the two channels. By the utilization of the buffers, the values are additionally averaged, to further reduce noise. The calibration loop is closed after the new offset settings are sent to the AFE. This sequence is executed until a minimum offset per channel and a minimum difference between the channels is reached.

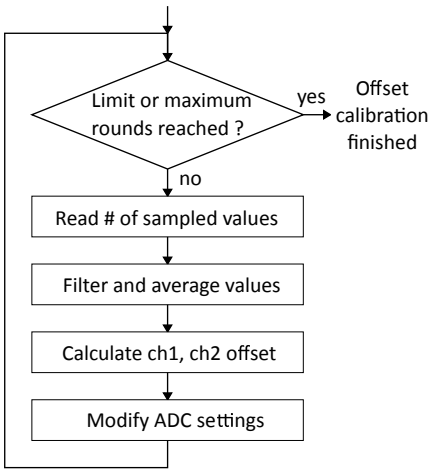

Figure 3.20.: Flow chart of the mixed signal dual channel offset calibration procedure.

The aim of the gain calibration is to equalize the two channels with respect to the measured amplitudes. Therefore, in Figure 3.21, the flow chart of the gain calibration is shown. Initially, both channels are sampled and a set of minimum and maximum values is stored. After the sampling period, by the usage of the averaged max and min values per channel $AV_{max,CHx}$ and $AV_{min,CHx}$, the difference Δ_{CHx} between them is calculated according to Equation 3.4:

$$\Delta_{CHx} = AV_{max,CHx} - AV_{min,CHx}. \tag{3.4}$$

The new AFE gain setting is calculated and subsequently set, through the calculation of the quotient of the two averaged values Δ_{CH1}, Δ_{CH2}. It is taken into account, that both channels do not exceed certain minimum or maximum limits for the gain setting. This procedure is finished, if both channels are equalized besides a small margin with respect to their amplitudes.

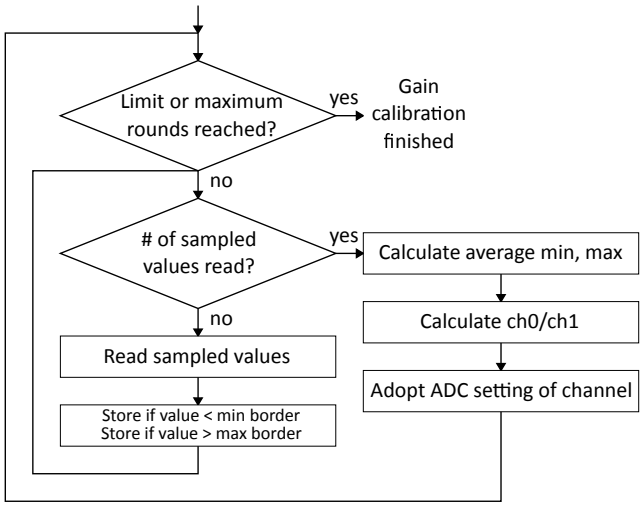

Figure 3.21.: Flow chart of the mixed signal dual channel gain calibration procedure.

Lastly the phase adjustment is performed, which is visualized in Figure 3.22. The phase adjustment is accomplished by sweeping through different phase settings between the two channels. Consequently, it is expected to get the phase relation between the two channels, which results into the minimum difference between them. Therefore, the first step is a raw phase calibration, where coarse phase setting steps are applied to pick out the region with the minimum channel difference. Subsequent to the raw calibration, the fine tuning is performed, whereby the previously found region is swept through by employing minimum phase settings steps. During the sampling stage, the absolute difference Δ_{phase} between the channels according to Equation 3.5 is evaluated. A circular buffer is used to reduce noise by averaging the Δ_{phase}.

$$\Delta_{phase} = |V_{CH2} - V_{CH1}| \tag{3.5}$$

3.8.2.2. Determination of the Resonance Characteristic

One of the required main functionalities of a photoacoustic based resonance sensor is the determination of the resonance frequency. As first step, it is

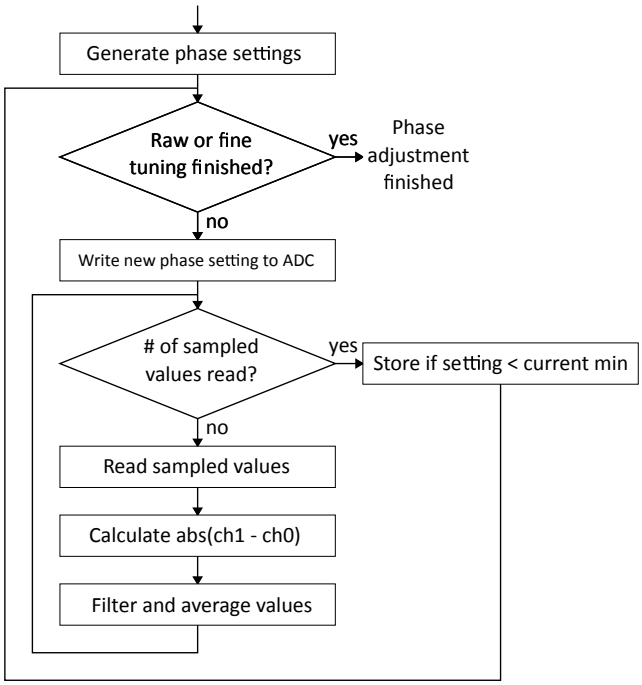

Figure 3.22.: Flow chart of the mixed signal dual channel phase adjustment procedure.

necessary to resolve the resonance frequency after assembling the cell, due to expected deviations from the simulation. Further, environmental factors like humidity or temperature (cf. Ishaku et al. [37]) do have an impact on the resonance frequency. Based on that, it is anticipated that periodically performed sweeps are required.
Figure 3.23 depicts the flow chart of the described resonance sweep procedure. The resonance sweep is performed by periodically adapting the frequency setting of the VCO, which does alter the modulation frequency of the used LED. After setting a new modulation frequency, the sampling step is completed. During this step, the reference signal values (cf. Section 3.5) and the microphone sensor values (cf. Section 3.6) are sampled. Subsequent, the two microphone signals are digitally subtracted and the resulting I and Q values are calculated as described in Section 2.1.2.5. The I and Q values are stored in circular buffers for subsequent filtering and are then individually summed up. The sampling is performed interrupt driven, since the external AFE ICs deliver end of conversion signals. After one sampling

period, the lock-in amplitude and phase are calculated and the frequency of the maximum amplitude is always stored.

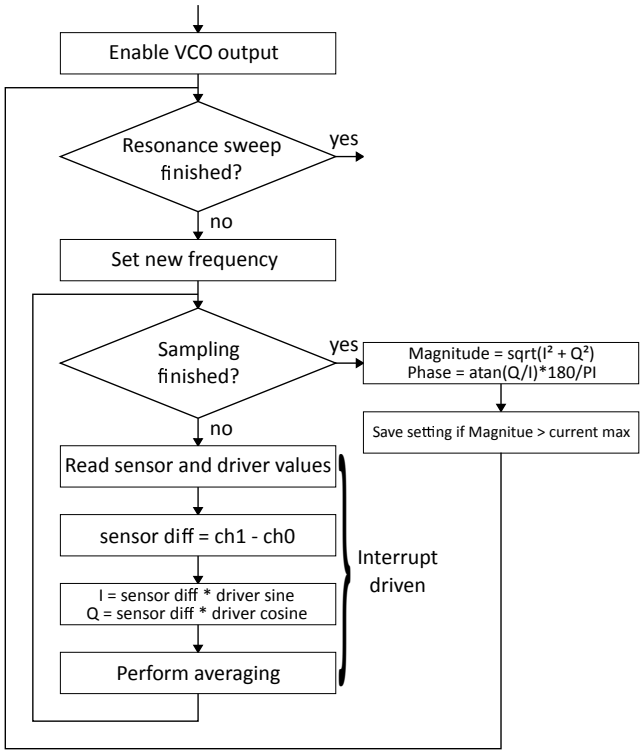

Figure 3.23.: Flow chart of the photoacoustic cell resonance sweep.

It is from importance, that the calculations performed during one sampling step, do not last longer than one sampling period. Otherwise the processing results into unpredictable behavior, since the defined steps can not be executed in time.

3.8.2.3. Procedure for Determination of the Concentration

The method to detect the concentration of the gas, is very similar to the determination of the resonance frequency, described in the previous section. Predominantly, the difference is that the modulation frequency remains the prior evaluated resonance frequency of the cell, to deploy the maximum

photoacoustic signal amplitude. Further, dependent on the detection mechanism, the beforehand measured background signal can be subtracted from the measured in-phase and quadrature components, as shown in Equation 3.6. This enhances the limit of detection in case of a stable background signal

$$\begin{aligned} I &= I_{meas} - I_{background} \\ Q &= Q_{meas} - Q_{background} \end{aligned} \tag{3.6}$$

3.9. LoRa Usage

In this last part of the methodology chapter, a brief overview of the LoRa usage within the sensor system is given. Long range (LoRa) is a LPWAN technology developed by Semtech. A theoretical introduction into the technology is provided in the attached paper (see A).

3.9.1. LoRa Transceiver SX1272

Within the sensor system, a LoRa SX1272 transceiver is utilized, to transfer the data to a central collection point. The SX1272 is used upon a STM32 Nucleo SX1272MB2xAS LoRa expansion board (schematic can be found in [38]), which comprises all necessary RF components for communication including antenna, antenna matching and filtering. The extension board can simply be attached to the STM32 Nucleo board (see section 3.8). In addition, the communication between 32 bit controller and the transceiver is realized with an SPI interface.
Generally speaking, LoRa is a spread spectrum technology. The characteristics of the technology (bandwidth, spreading factor of the chirps, code rate, transmission power) are adjustable (see appendix A or [39, 40]). Different LoRa transceivers exist. The SX1272 transceiver features a maximum transmission power of 14 dBm and a sensitvity down to -137 dBm, dependent on the parameter setting. Strongly related to the parameter setting and the

environment, a communication distance of up to several kilometers can be reached (cf. appendix A or [40]).

3.9.2. Utilization in mbed

From a software point of view, the LoRa communication is part of the mbed application (see Figure 3.19). It is based upon the SX1272Lib mbed library provided by Semtech. This library features most functionalities implemented by the SX1272 transceiver. Consequently, for transmission or receiver mode, only an initialization of the library and the device itself is required. The library features an event based mechanism, where different tasks can be executed, dependent on which event happened. This can for example be a task for setting the device into sleep mode, after successful transmission. The transmission of data can be implemented by a simple send method. Furthermore, it is possible to receive data for certain periods of time, respectively it is feasible to enable the receiver in continuous mode, as used within the distance measurements in the attached paper (see A). Within this work only elementary functions for initialization, sending and receiving were implemented, which were used during the distance measurements.

4. Results and Discussion

In this chapter results are presented and challenges of the implementation are discussed. First, the signal generation circuit is analyzed. Thereafter it is focused on the microphone channel calibration from Section 3.8.2.1. This is followed by the resonance characteristic of the photoacoustic cell. Subsequently, the sensor is evaluated, whereas the sensor response for different nitrogen dioxide concentrations is shown. Moreover, in Section 4.4.2, the limit of detection of the sensor unit is evaluated. Finally power consumption considerations are discussed.

4.1. Signal Generation Verification

The signal generation part of the sensor, which was already introduced in Section 3.5, is responsible to provide the driving signal for the light source (cf. Section 3.2.1) and the reference signal for the LIA (cf. Section 3.7). In Figure 3.12, the block level diagram of the signal generation circuit is shown. The evaluation of the reference signal is from necessity, due to the importance of the LIA signal detection. Impurities in the signals deteriorate the detection and gather spectral noise components.
Figure 4.1 depicts the two rectangular signals, measured at the output of the I-Q generator. As expected, it can be seen, that the two rectangular signals are 90° phase shifted. Subsequently, the signals are low-pass filtered, to obtain only the fundamental frequency of the square wave. The filtered signals measured by an oscilloscope are illustrated in Figure 4.2.
From main interest is thereby, if all frequency components beside the fundamental frequency are properly canceled. Therefore, the FFT from the time domain sine signal in Figure 4.2 is depicted in Figure 4.3. The fundamental frequency ($\sim$2.25 kHz) raises above all other components, with a factor of

at least 40 dB in between. The first harmonic frequency at about 4.5 kHz is damped by approximately 45 dB, whereby according to the datasheet of the low-pass filter LTC1069-1 (cf. [41]) a reduction of 55 dB was expected. The 10 dB difference can on the one hand be referred to inaccuracies in the FFT of the oscilloscope. On the other hand, the spectral signal position is only slightly below the cut off frequency of the filter (-0.7 dB) and additionally, deviations from the theoretical performance are expected.

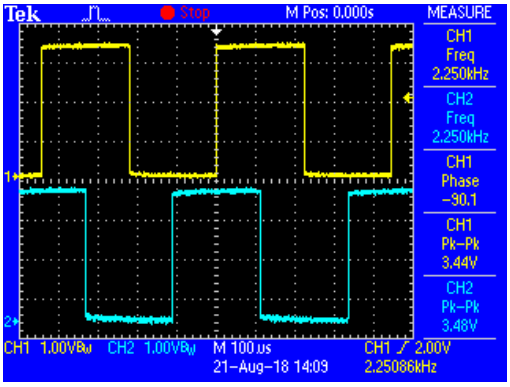

Figure 4.1.: Square wave and quadrature square wave generated out of the oscillator output.

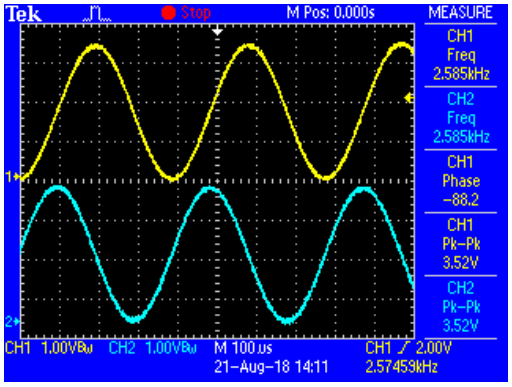

Figure 4.2.: Sine wave and cosine wave after filtering the rectangular waves by the usage of an 8th order low-pass filter.

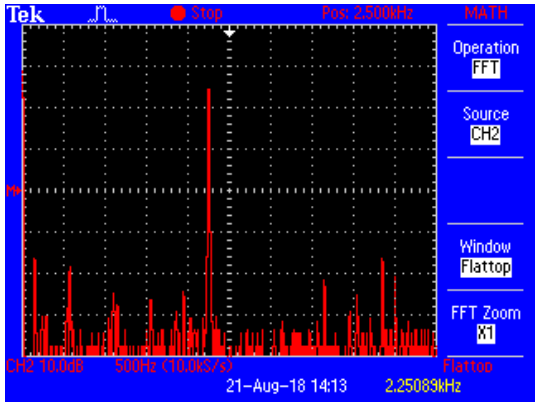

Figure 4.3.: FFT of the sine wave which is used as modulation source for the LED and as reference signal for the LIA.

The adjustment of the frequency setting of the VCO works as expected.

Minimum frequency steps around 2.25 kHz are slightly below 0.5 Hz, which is sufficient enough for precise resonance detection.
Overall, it can be said that the reference signal generation circuit performance is as expected, although improvements are possible within the purity of the reference signals.

4.2. Evaluation of the Microphone Channel Calibration

Previous chapters dealed with techniques for noise canceling, by using two identical resonators to enhance the resolution of the sensor. This requires on the one hand a very sensitive selection of the measurement components and on the other hand a properly designed solution. Especially the selection of the microphones is very critical due to manufacturing differences in the electronic parts of the microphones. These differences, mainly in the internal preamplifier stages of the microphones, result in phase and gain variances, which have a strong impact if noise canceling is applied.
The first described amplification and conversion circuit (cf. Section 3.6.1) processed the signals purely analog. It was learned, that due to production variances, especially within electret microphones, the output signals of the microphones bring along a phase shift by several degrees and gain variations above 10 percent. By directly subtracting the signals with an instrumentation amplifier, no improvements could be achieved through noise canceling, mainly due to the phase shift, which is at least in analog manner difficult to compensate.
Consequently, the second approach was to treat the two microphone channels separately (cf. Section 3.6.2). The amplification and conversion to the digital domain is individually performed. Thereafter, the utilized AFE (see Figure 3.16) is used to adjust the two microphone channels in case of voltage offset, gain and phase shift. Implementation-wise was this achieved through three calibrations routines (cf. Section 3.8.2.1). These calibration routines are applied to the background signal without exciting the sensor with the LED-source.
Firstly, the offset calibration adjusts the signal to be centered around the

x-axis, by gradually determining the average value of each channel and adjusting the internal offset value of both channels in the AFE. One applied measurement cycle is illustrated in Figure 4.4. Both channels are shown, which initially differ by about 90 LSB and are finally equalized.
Secondly, the gain calibration is performed. This is done by collecting a set of minimum and maximum values of both channels and thus calculating the peak to peak amplitude. The amplitudes of both channels are possibly matched, by adjusting the gain of both in a stepwise adaption. One sample measurement outcome is shown in Figure 4.5.

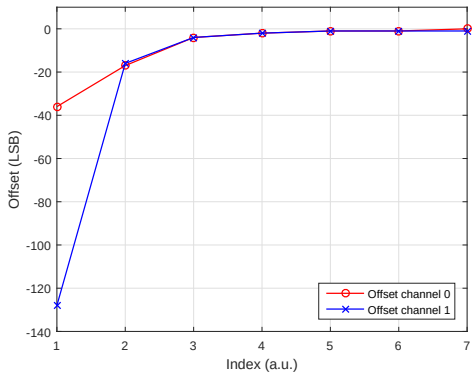

Figure 4.4.: Offset calibration of the two microphone channels to minimize the voltage offset.

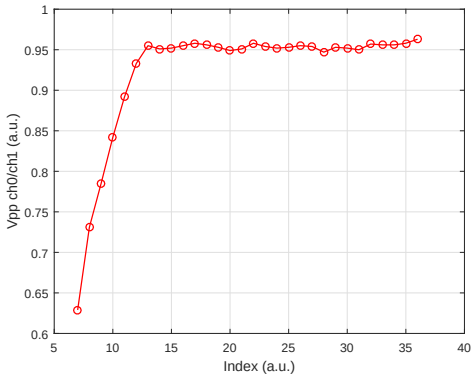

Figure 4.5.: Gain calibration of the two microphone channels to minimize the gain difference.

Thirdly, the phase calibration is conducted. This is done by sweeping through different phase settings of the AFE and calculating the difference between the two channels, to find the minimum. By applying this method, Figure 4.6 depicts the outcome of a phase calibration sweep. Compared to the calculated, expected curve, which is shown in Figure 4.7, only a trend can be observed, owing to strong variations in the measurement. It is expected, that the background signal is too weak to get a proper curve, at least for the used averaging period per phase setting (about 1.5 s). Improvements are expected by enlarging the averaging time, or by applying a background signal, for example through a loudspeaker.

Summarizing, it can be said that the offset and gain calibration deliver the expected results, by matching the two channels in these two characteristics.

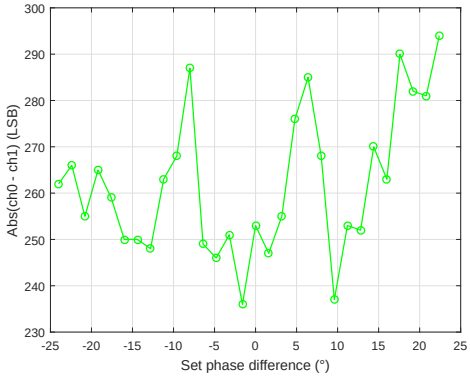

Figure 4.6.: Result of a phase calibration run of the two microphone channels.

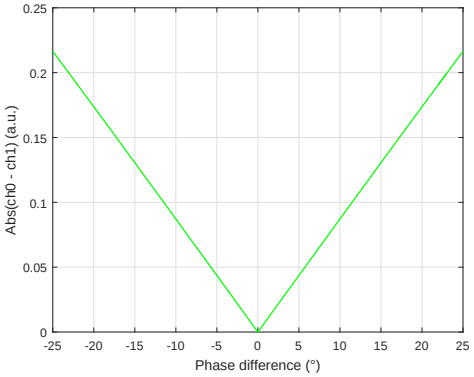

Figure 4.7.: Expected result of the phase calibration.

Opposed to that, the adaptions using the phase calibration routine strongly vary and no reliable phase shift compensation could be achieved up to now.

4.3. Resonance Characteristic of the Photoacoustic Cell

Of great importance within the photoacoustic sensor are the determination and tracking of the resonance frequency. As described in the previous chapter (see Section 3.8.2.2), it is from necessity to capture the actual resonance frequency after manufacturing, owing to deviations compared to simulations and pre-calculations. In addition, it is required to track the resonance frequency for the long term employment, based on changing environmental conditions (humidity, temperature).
In Figure 4.8, the resonance curve of the constructed resonance cell is shown. The evaluation was performed by applying a sweep over the modulation frequency. This sweep was carried out with a nitrogen dioxide concentration of 200 ppm. In blue, the resonance curve of the cell is shown. The quality factor Q was determined with a value of 23. Additionally to the amplitude, the

phase was captured, which has a zero-crossing at resonance. The resonance frequency was determined at 2260 Hz. This value deviates on the one hand by 150 Hz, compared to the simulation result from Section 3.4.1 with 2110 Hz. On the other hand the chosen value of 2200 Hz from Equation 3.1 differs only by 60 Hz. This deviations can be referred to manufacturing variances, due to the fact that the cell was manually assembled and shortcomings of the simulation and the analytical model.

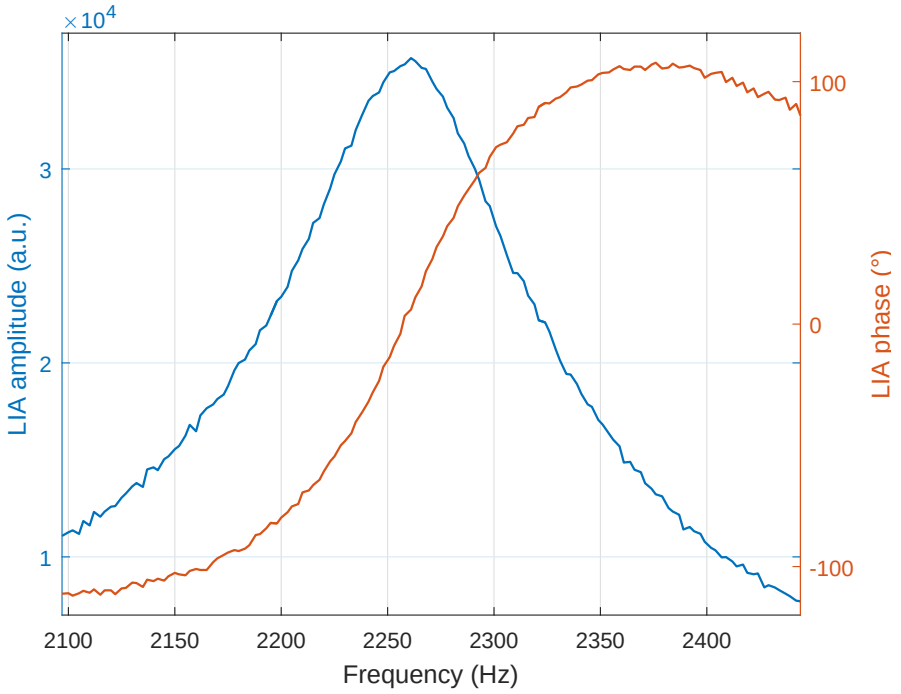

Figure 4.8.: Resonance characteristic of the photoacoustic cell including LIA amplitude and phase.

Generally speaking, the deviations are acceptable and were expected to that extent. The following measurements on the next pages are evaluated at the resonance frequency, to capture the maximum acoustic wave.

4.4. Sensor Evaluation

After dealing with the signal generation verification and the resonance characteristic of the cell, the evaluation of the sensor follows. The evaluation was performed in the laboratory of the Institute of Electronic Sensor Systems (IES), at the Technical University of Graz. The procedure conducted with the laboratory setup is illustrated in Figure 4.9.

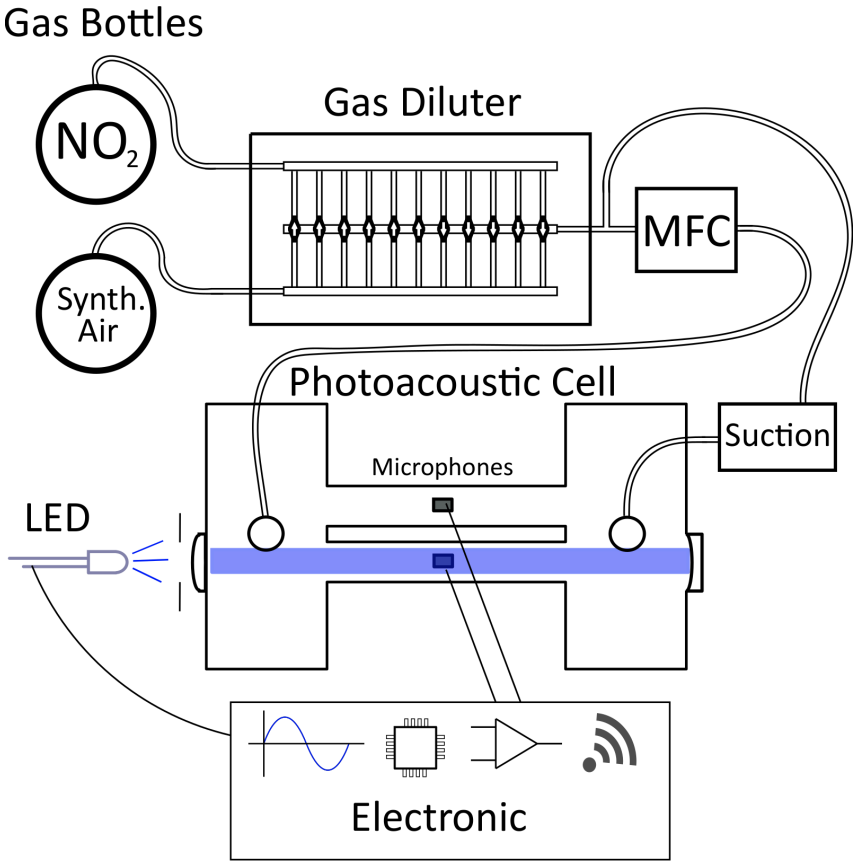

Figure 4.9.: Schematic of the laboratory setup, which was used to evaluate the sensor. NO_2 and synthetic air gas bottles are connected via pressure regulators to a gas diluter. The gas flow is controlled by a MFC, before the gas enters the cell. Exiting the cell, the gas is removed through the laboratory suction.

To test different gas concentrations within the sensor system, a reference nitrogen dioxide gas bottle with 19.2 ppm from Messer Austria GmbH

was utilized. NO_2 was diluted with synthetic air from Messer gases (see technical datasheet [42]), with a maximum contaminant of 10 ppb nitrogen dioxide. The dilution was done by a in-house built gas diluter (cf. Breitegger et al. [43]). By the utilization of the diluter a minimum NO_2 concentration below 20 ppb is achievable with the used reference. Subsequently to the gas diluter, a mass flow controller (MFC) is deployed to set the gas flow through the PA cell. For all measurements a gas flow of 0.3 l/min was set. Due to acoustic noise generated by the MFC an acoustic filter is placed between MFC and the gas port of the cell, which is not sketched in the figure. The second gas port of the PA cell is connected to the laboratory suction. The remaining parts of the figure belong to the sensor itself (described in Chapter 3). Additionally, Figure 4.10 and Figure 4.11 show the sensor during operation in the laboratory.

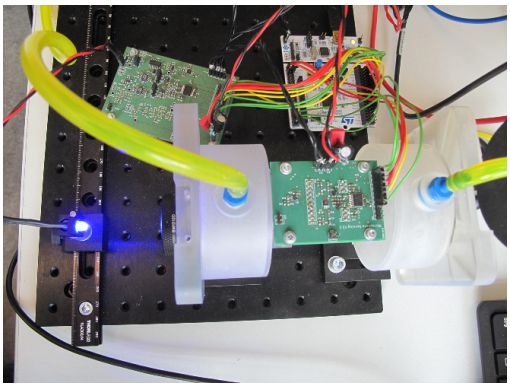

Figure 4.10.: Top view of the sensor operated in the laboratory.

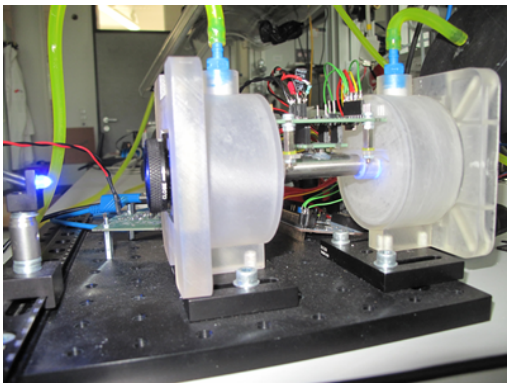

Figure 4.11.: Lateral view of the sensor operated in the laboratory.

4.4.1. Nitrogen Dioxide Measurements

Different nitrogen dioxide concentrations between 1.2 ppm and 19.2 ppm were measured. First, the measurements were conducted by the usage of the photoacoustic signal of the excited resonator only (single ended). Second, differential measurements were carried out. Thereby, the background signal from the second resonator, is subtracted from the excited resonator.

Prior to the differential measurement, the described calibrations were performed. The integration time of the sensor was set to 20 seconds. This integration time is composed out of 2 seconds accumulation of the values and subsequently applying a low-pass filter to the integrated values.

4.4.1.1. Single Ended

The outcome of a single ended concentration measurement over time is shown in Figure 4.12.

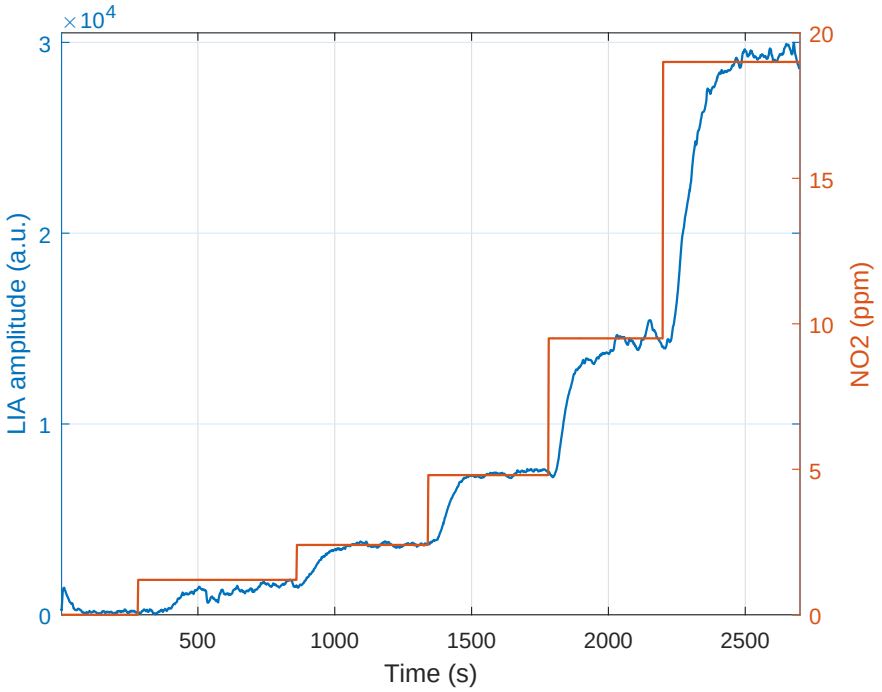

Figure 4.12.: Single ended measurement of different NO_2 concentrations over a period of time. The NO_2 concentration is therefor compared to the calculated LIA amplitude (phase corrected), using only the excited resonator.

Initially the concentration was set to 0 ppm and was subsequently increased up to 19.2 ppm. The blue signal depicts the processed, phase corrected sensor response of the controlling unit. In addition, the orange curve shows

the employed NO_2 concentration. Phase corrected in this context means, that the signal, which is observed during 0 ppm NO_2 concentration (background noise), is subtracted from the resulting signal (see Section 3.8.2.3). Consequently, the sensor signal, which measures only synthetic air, is moved to the x-axis without offset. Each concentration was set till the sensor signal stabilized. Comparing the set concentration to the sensor response, a delay can be observed. First this delay is accounted to the gas diluter. It takes time, especially at low concentrations, till the actually employed concentration appears at the exit of the diluter. Second, some time is required till the volumes of the cell and the prior positioned acoustic buffer are filled. Third, the set integration time of 20 seconds adds an additional delay.
It can be seen, that the sensor response fits quite well to the set concentration. Slight deviations can be observed. First, they can be referred to inaccuracies of the sensor signal processing and second to uncertainties of the gas diluter. In addition, temporal variations of the sensor response are observed, such as above 2000 seconds within 9 ppm and above 2400 seconds within 19.2 ppm. These might occur to variations of the gas flow.
Supplemental to the evaluation over time, the sensor response function was evaluated. Therefor, all set concentrations were averaged for several minutes. In Figure 4.13, the sensor responses are opposed to the nitrogen dioxide concentration. The blue measurements depict the direct sensor response, whereas the red ones feature the phase corrected sensor response. A linear curve is fitted through both measurements. It can be seen, that both lines fit well through the plotted points, which reflect the expected linear sensor response. This is due to the fact, that NO_2 and the background (synthetic air) have in this case the same phase. Within the plotted amplitudes, the calculated variations are drawn. They depict in x-direction the uncertainties of the gas diluter and in y-direction the variations of the averaged signal. If the variations in x and y direction are included, all measurements fit onto the linear response of the sensor. Further, no real difference between direct sensor signal and phase corrected response is observed.

4.4.1.2. Differential

Following the single ended evaluation, this part represents the differential evaluation of the sensor. In the differential mode, the signal from the second,

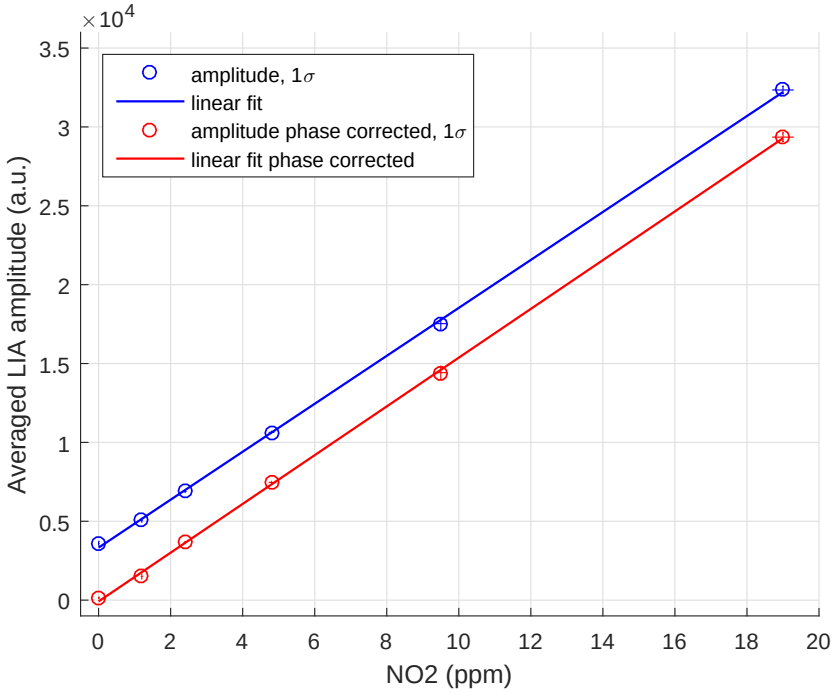

Figure 4.13.: Single ended, averaged LIA amplitudes (with and without phase correction) for several NO_2 concentrations, including standard deviations, using only the excited resonator. A linear function was fitted through the calculated amplitude values.

unexcited resonator is subtracted from the signal of the excited resonator. The measurement was accomplished with the same settings as within the previous, single ended assessment. Consequently, the nitrogen dioxide concentrations are successively increased from 0 ppm to 19.2 ppm.
Figure 4.14 represents the differential sensor evaluation over time. Conferring the adjusted concentration to the sensor response, substantial differences compared to the single ended outcome can be observed. In principle the sensor response fits to the set concentration, nevertheless, sizeable deviations can be determined.

Additionally, the sensor response function for the differential mode of the sensor is evaluated. The outcome is illustrated in Figure 4.15, where the blue measurements show again the direct sensor response and the red markings

represent the phase corrected result. Noticeable deviations from a linear function of the direct sensor response, can be observed.

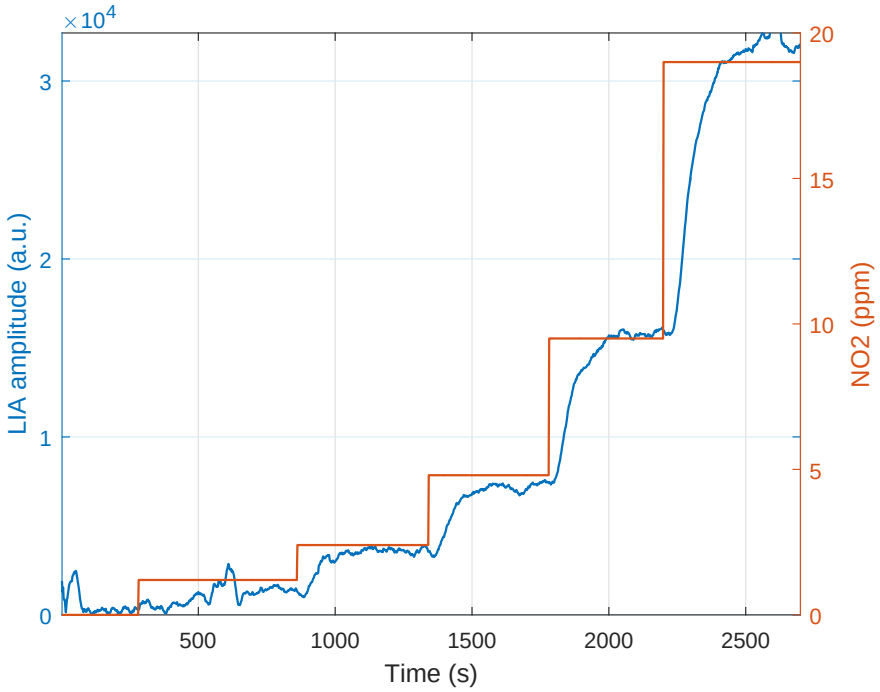

Figure 4.14.: Differential measurement of different NO_2 concentrations over a period of time. The NO_2 concentration is therefor compared to the calculated LIA amplitude (phase corrected), using both microphones.

On the one hand, this can be referred to different phases of the analyte gas (NO_2) and the background. On the other hand, the non-linear behavior can be attributed to the phase shift, which emerges through the manufacturing variances of the microphones and to the non functional phase calibration mechanism (see Section 4.2). The phase corrected response shows a predominant linear behavior, whereby most points fit onto the linear line, including the drawn variations in x and y direction. Due to the existing phase shift, the noise canceling does rather have a negative impact on the final signal, than the expected subtraction of the background signal.

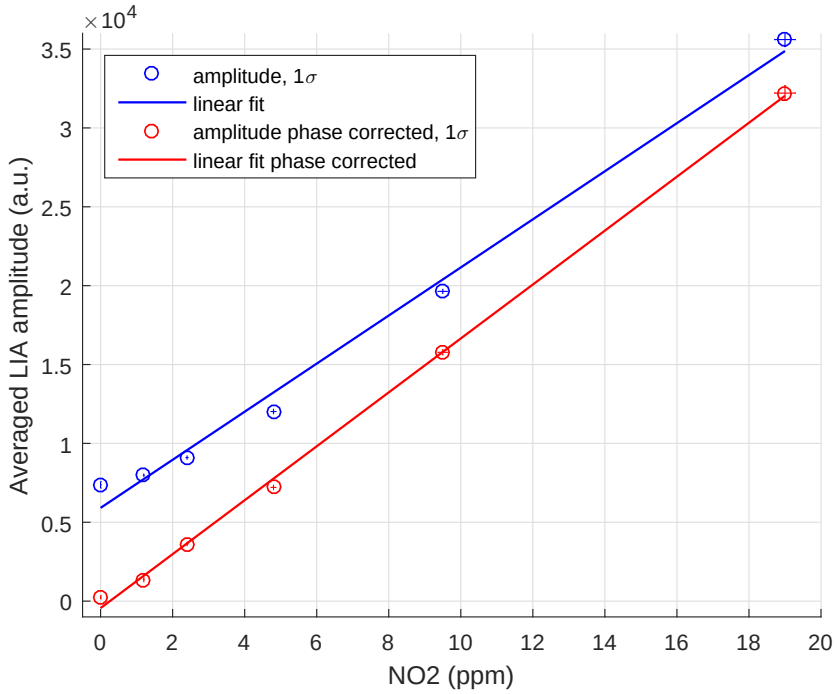

Figure 4.15.: Differential, averaged LIA amplitudes (with and without phase correction) for several NO_2 concentrations, including standard deviations on both axis. A linear function was fitted through the calculated amplitude values.

4.4.2. Limit of Detection

Supplementary to the evaluation over time and the sensor response function, the limit of detection (LOD) of the sensor is assessed in this section. This was done by evaluating the standard deviation of the sensor response, together with the sensor response function. Considering that, the Allan Variance (cf. [44]) of the background signal (without NO_2, only synthetic air) was calculated, opposed to the integration time. In Figure 4.16, the corresponding background signal is shown. The signal was therefor captured for about 1700 seconds. The LOD was only evaluated for the single ended sensor mode.

In general, the Allan Variance is used to measure the frequency stability and was mainly applied in the evaluation of oscillators and amplifiers.

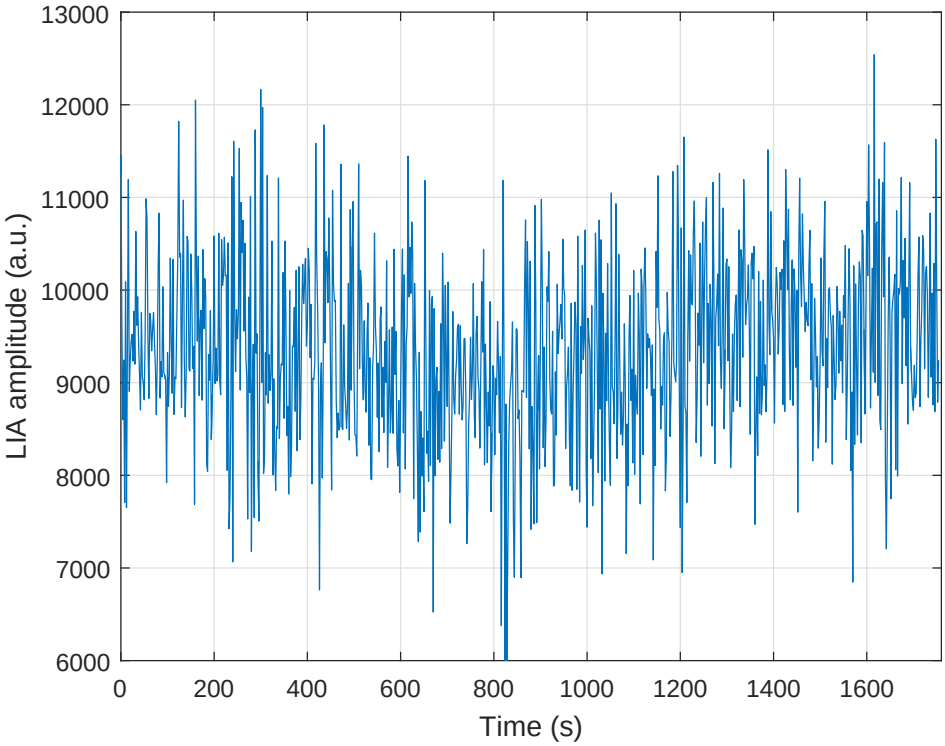

Figure 4.16.: Measurement of the background signal, with only synthetic air flowing through the photoacoustic cell, by the usage of the single ended mode of the sensor. LIA integration time was 2 seconds.

However, it can also be utilized to evaluate the long term stability of signals. In this case, it is used to determine the LOD of the sensor, dependent on the integration time. The outcome is the integration time with the minimum variation of the sensor signal.
The Allan Variance was evaluated with a Matlab script and is represented in Figure 4.17.

On the x-axis, the integration time of the sensor in logarithmic scale is shown. The y-axis represents the standard deviation σ of the background signal. By contemplating the curve it can be seen, that the first minima is reached between 100 and 200, with 124 seconds integration time. After this minima the curve rises again due to the long term drift of the signal.

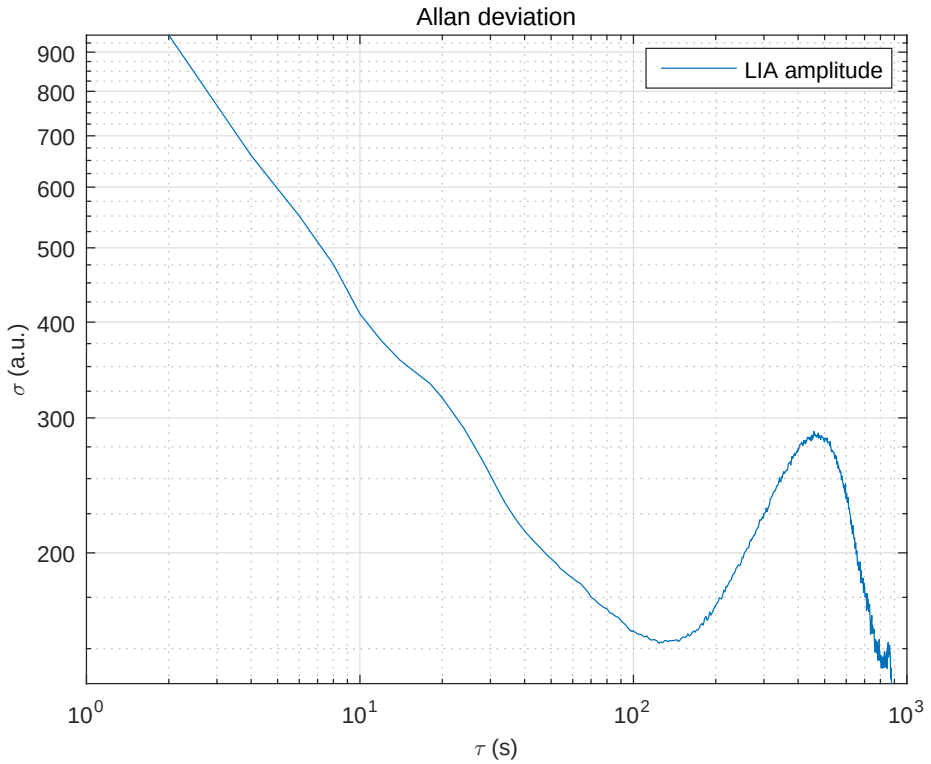

Figure 4.17.: Allan Deviation of the background signal from Figure 4.16. The minima indicates the integration time with the minimum variation of the signal.

The second minima can be ignored due to the fact, that the integration time converges to the acquisition time of the signal. With the utilization of the minimum variance of 152.5, the LOD can be calculated to 101 ppb according to the linear Equation 4.1 for the single ended detection with phase correction:

$$LOD = \frac{\sigma(\tau)}{k} = \frac{152.5}{1545.54} \mid_{\sigma=152.5,\tau=124} = 0.10ppm. \tag{4.1}$$

Within Equation 4.1 LOD specifies the limit of detection for the single ended sensor mode. In addition, the standard deviation $\sigma(\tau)$ is dependent on the integration time τ and the slope k of the linear function. By the utilization

of Equation 4.1 different limit of detections, for different integration times and multiples of the standard deviations, are presented in Table 4.1.

Limit of Detection (in ppm)				
2 s integration, 1 σ	2 s int., 3 σ	20 s int., 1 σ	20 s int., 3 σ	124 s int., 1 σ
0.63	1.90	0.23	0.68	0.1

Table 4.1.: Limit of detection shown for different properties of the sensor in single ended mode.

Comparing this values, the LOD varies between 1.93 ppm and 101 ppb dependent on the integration time and the standard deviation σ. For applying the sensor in real life application, it must be considered, that the sensor response time increases with growing integration time. Nevertheless, the sensor gets more accurate with increasing integration time. An appropriate choice must be made dependent on the utilization of the sensor. For environmental sensing, the integration time can well be up to 100 s. However, the long integration time has a negative impact on the power consumption of the sensor, which can be from significance, if the sensor is battery operated. With an integration time of 124 seconds and a LOD of 101 ppb, EU [23] or WHO [2] limits can only be roughly assessed. This can still be enhanced by the usage of a LED with higher output power, based on the proportional dependency on the PA signal (see Equation 2.1).

4.5. LoRa Range Measurements

The results of the LoRa range measurements can be found in the attached paper A.

4.6. Power Consumption Considerations

In this last part of the chapter, the power consumption of the sensor is considered. The sensor concept is designed to be a low power design. Accordingly, low power electronic parts were best possibly chosen. First,

an ultra low power microcontroller was selected as central processing unit. Second, the signal generation (see Section 3.5) and both signal amplification and conversion circuits (see Section 3.6) are designed, with the utilization of low power components. Both circuit concepts have power management ICs, which are able to shutdown the current consumption, controlled by the microcontroller.
In Table 4.2 the measured power consumption of each major electronic block is shown during sensing operation. The microcontroller consumes 15.6 mA during full speed operation with 80 MHz clock frequency, whereby several peripherals like SPI, timer and memories are enabled. In addition, the signal amplification and conversion circuit (solution 2) dissipates 6.2 mA. The principal consumer is the signal generation block, including the PA light source with 81.3 mA, whereby 46.9 mA are dissipated by the LED. Consequently, the sensor dissipates 103.1 mA during full operation. The signal generation and signal amplification and conversion blocks, both together, consume during shutdown mode 400 μA.

Electronic Component	Comment	Measured Consumption (in mA)
Microcontroller	STM32L476, Nucleo board CPU speed 80 MHz, including peripherals	15.6
Signal generation	Including LED consumption	81.3
Signal generation	Without LED consumption	34.4
Signal amplification and conversion	Solution 2	6.2

Table 4.2.: Measurement of the power consumption of the different electronic sensor parts.

In Figure 4.18 the measured power consumption of the individual electronic blocks, including the LED, is visualized. Nearly half of the power is consumed by the LED. The remaining part is dissipated by the electronic components.

A closer look at the power consumption of each block is taken in Table 4.3. The measured values are therefor compared to the estimated values from datasheets (typical consumption) and calculations. The CPU itself running at

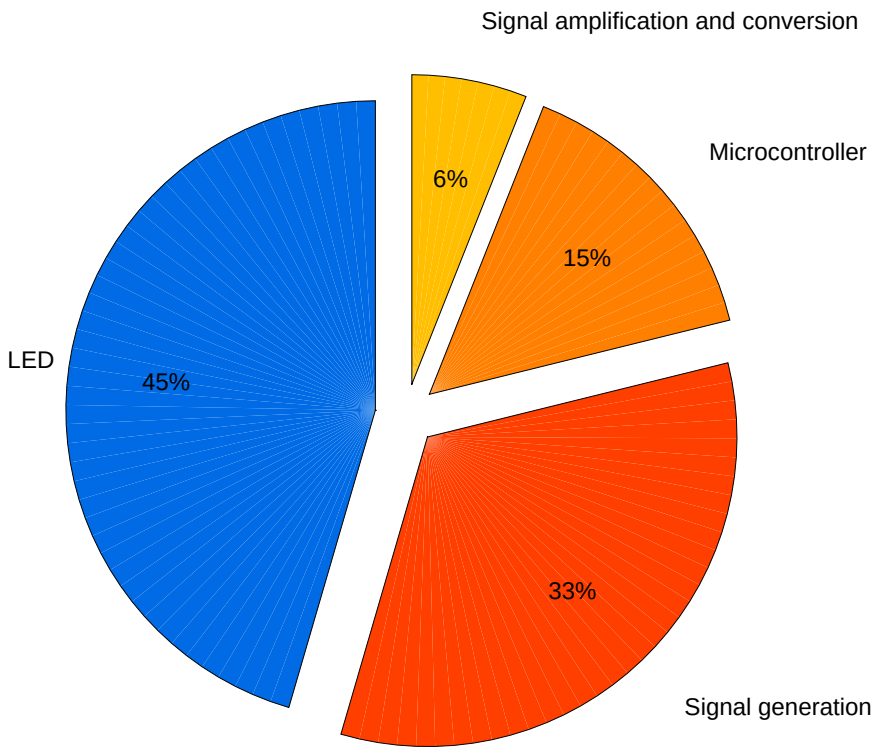

Figure 4.18.: Measured power consumption distribution during sensing operation of the individual electronic parts (including the LED).

80 MHz consumes 10.2 mA according to [45]. Additionally, several required peripherals are included, like static random access memory (SRAM), SPI or timers and dissipate 5.2 mA, which results in a total calculated consumption of 15.4 mA.
The current drain of the signal generation block without LED was calculated to 30.1 mA. Thereby, the majority is dissipated by the sampling part of the circuit. This comprises the signal conditioning for the AFE, the reference voltage circuit for the AFE and the AFE itself. A large part is consumed by the signal generation sub-circuit, where both (for sine and cosine signals)

8th order low-pass filter together dissipate 7.6 mA. The estimated value deviates by about 4 mA compared to the measured consumption of the circuit. This can on the one hand be referred to variations of the typical power consumption values and on the other hand to minor not included electronic parts.
The estimated power dissipation of the signal amplification and conversion (solution 2) block is 6.1 mA. In this case, the vast amount is consumed by the AFE with 5.1 mA.

Electronic Component	Sub Component	Measured Consumption (in mA)	Estimated Consumption (in mA)
Microcontroller		15.6	15.4
	CPU @ 80 MHz	-	10.2
	Specific peripherals SRAM, SPI, Timer, BUS Matrix, AHB-, APB bridge	-	5.2
Signal generation without LED		34.4	30.1
	Power Mgmt.	-	0.8
	Signal Generation	-	7.8
	Sampling	-	20.5
	LED Driver	-	1.0
Signal amplification and conversion Solution 2		6.2	6.1

Table 4.3.: Comparison of estimated and measured power consumption of the individual electronic sensor blocks.

Considering the total power consumption, improvements in case of power reductions are possible. Mainly the signal generation block and the microcontroller consumption can be diminished. It needs to be investigated, which of the enabled peripherals are required. In addition, the clocking scheme

of the controller requires investigations, since the power dissipation can be reduced by lowering the clock of specific domains. The main dissipation is consumed by the signal generation circuit. Enhancements can principally be made within the signal conditioning of the AFE and by replacing the low-pass filters of the signal generation part.
Finally, the power dissipation of the utilized SX1272 LoRa transceiver was measured during both modes (transmit, receive) of operation. The measured values, compared to the estimated values determined from the SX1272 datasheet (see [46]) and by the usage of the LoRa modem calculator tool (description can be found in [47]) are represented in Table 4.4. In addition, the transmission power was set to 14 dBm. The measured power dissipation comprises the full LoRa Nucleo shield (see schematic [38]) including antenna RF switch and ultra high speed (UHS) inverter. As expected, does the transmitter mode consume more power compared to the receiver mode. The measured transmitter dissipation fits to the estimated power consumption. However, a strong deviation from the estimated receiver consumption can be determined. Most likely, this can be referred to the on-board RF switch and UHS inverter.

LoRa mode	Measured Consumption (in mA)	Estimated Consumption (in mA)
Transmit (14 dBm)	42.0	44.0
Receive	27.0	10.8

Table 4.4.: Comparison of measured and expected LoRa (SX1272, Nucleo shield) power consumption, according to the SX1272 datasheet.

5. Conclusion and Outlook

In this work the design of a low-power, photoacoustic based nitrogen dioxide sensor, with wireless sensor capability was presented. Subsequently to the introduction, the theoretical basis of the sensor design was provided (cf. chapter 2). First, the commonly utilized low cost sensor technologies (MOS and EC) were introduced. They protrude by their low production costs, small size and the low detection limits, but suffer from cross sensitivity, long term drift and dependency on environmental conditions. Next, the foundation to PAS was provided. This comprised a short description of the photoacoustic effect followed by a theoretical primer on PA cell design. The theoretical introduction further included the detection of NO_2 and influences of other gases, the acoustic detection of the resulting pressure wave and finally the necessary signal processing fundamentals.
In the ensuing methodology chapter (3) the sensor design was presented. Initially, an overview of the system design was given, which was concluded by the description of the individual parts of the sensor. This comprised first the optical components for the collimation of the LED beam and the selection of the microphone, respectively the design of the differential PA cell. Thereafter the electronic parts of the sensor were presented, including signal generation and the amplification and conversion circuits. The final part of the methodology chapter described the software implementation of the LIA, the overall software structure and the utilization of LoRa.
Finally evaluation results of the sensor were discussed (cf. chapter 4). Issues within the phase calibration of the channels, hampered the differential mode of the sensor. This was owed to manufacturing differences of the utilized microphones and the subsequent issues within the background noise cancellation. Nevertheless, by using the single PAS mode of the sensor, a linear sensor response and a LOD down to 101 ppb could be achieved. In the concluding part of the results, the power consumption of the sensor was discussed, whereby approximately 50 percent of the power is dissipated by

the LED light source.
Overall can be said, that the expected results have been achieved, especially in case of sensor response and limit of detection. Although, to transfer the sensor prototype into a fully functional device, various evaluations and enhancements are still necessary, which can be addressed in future work.
First, statistical evaluations are required to properly verify the sensor response. Of particular importance are field measurements. Often sensors achieve good results within laboratory measurements, but show badly deteriorated behavior due to the influence of changing environmental conditions or cross influences in field evaluations (cf. [7, 48, 49]). In addition, a concurrent measurement with a reference equipment is of particular importance, to confirm the research outcome.
To further develop the sensor, several improvements can be considered. The photoacoustic cell can be reduced by up to a factor of four. This will decrease on the one hand the sensor size and on the other hand increase the resonance frequency of the cell. Contemplating the currently utilized electret microphones, frequencies up to 6 kHz can be handled. Moreover, enhancements within the cell construction are feasible. The cell can either be entirely printed, or milled out of a metal compound.
Another aspect for improvements are the electronic components. A single PCB comprising all parts is achievable. Simplifications within the signal generation part are feasible, whereby the used VCO and filter stages can be replaced by a on-chip pulse width modulation (PWM). The reference sine and cosine could be digitally calculated, according to the PWM. In addition, power dissipation enhancement are practicable, as described in section 4.6.
In terms of current sensor functionality, the differential mode requires proper evaluation. It has to be investigated, what the exact issues within the phase calibration are. Additionally, an improvement of the LOD can be expected, if the phase calibration can be rectified.
Finally, to monitor the short term limit (see Table 1.1) set by the WHO [2] or the EU [23] of 21 ppb, a LED with higher optical output power can be utilized.

Bibliography

[1] Transport & Environment. *Dieselgate: Who? What? How?* Study. Transport & Environment, 2016. URL: https://www.transportenvironment.org/sites/te/files/2016_09_Dieselgate_report_who_what_how_FINAL_0.pdf (visited on 10/12/2018) (cit. on p. 1).

[2] World Health Organization. *WHO Air quality guidelines for particulate matter, ozone, nitrogen dioxide and sulfur dioxide*. Report. WHO, 2005 (cit. on pp. 1, 2, 60, 66).

[3] World Air Quality Index Project. URL: http://aqicn.org/ (visited on 10/16/2018) (cit. on p. 1).

[4] Ministry of Environment and Sustainable Development Dakar - Senegal. URL: https://asic.aqrc.ucdavis.edu/sites/g/files/dgvnsk3466/files/inline-files/Saliou%20Souare%20-%20Pr%C3%A9sentation_saliou_souare%2016x9.pdf (visited on 10/16/2018) (cit. on p. 1).

[5] Philip J.D. Peterson et al. "Practical Use of Metal Oxide Semiconductor Gas Sensors for Measuring Nitrogen Dioxide and Ozone in Urban Environments." In: *sensors* 17 (7 2017). DOI: 10.3390/s17071653 (cit. on p. 4).

[6] Anuj Kumar, Hiesik Kim, and Gerhard P. Hancke. "Environmental Monitoring Systems: A Review." In: *IEEE Sensors* 13 (4 2013). DOI: 10.1109/JSEN.2012.2233469 (cit. on p. 4).

[7] Aakash C. Rai and Prashant Kumar. *Summary of air quality sensors and recommendations for application*. Report. iSCAPE, 2017 (cit. on pp. 4, 66).

[8] Alastair C. Lewis et al. "Evaluating the performance of low cost chemical sensors for air pollution research." In: *Faraday Discussions* (2016). DOI: 10.1039/C5FD00201J (cit. on p. 5).

[9] Harald A. Beck. "Anwendung der Photoakustischen Spektroskopie in der Prozess-und Umweltanalytik." Dissertation. Fakultät für Chemie, Technische Universität München, 2003 (cit. on p. 6).

[10] Thomas Rück, Rudolf Bierl, and Frank-Michael Matysik. "Low-cost photoacoustic NO2 trace gas monitoring at the pptV-level." In: *Sensors and Actuators A: Physical* 263 (2017). DOI: 0.1016/j.sna.2017.06.036 (cit. on pp. 6, 13).

[11] G. R. Lima et al. "Sensitive harmonic detection of ammonia trace using a compact photoacoustic resonator at double-pass configuration and a wavelength-modulated distributed feedback diode laser." In: *Applied Physics B* 117 (1 2014). DOI: 10.1007/s00340-014-5840-z (cit. on p. 6).

[12] Ralf Bauer et al. "A 3D-printed miniature gas cell for photoacoustic spectroscopy of trace gases." In: *Optics Letters* 39 (16 2014). DOI: 10.1364/OL.39.004796 (cit. on pp. 6, 13).

[13] Michael Köhring et al. "LED-Absorption-QEPAS Sensor for Biogas Plants." In: *sensors* 15 (5 2015). DOI: 10.3390/s150512092 (cit. on pp. 6, 11).

[14] T. Kuusela et al. "Photoacoustic gas detection using a cantilever microphone and III–V mid-IR LEDs." In: *Vibrational Spectroscopy* 51 (2 2009). DOI: 10.1016/j.vibspec.2009.08.001 (cit. on pp. 6, 12).

[15] Jaakko Saarela et al. "Phase-sensitive method for background-compensated photoacoustic detection of NO2 using high-power LEDs." In: *Optics Express* 19 (S4 2011). DOI: 10.1364/OE.19.00A725 (cit. on p. 6).

[16] Mikael Lassen et al. "Photoacoustic spectroscopy of NO2 using a mid-infrared pulsed optical parametric oscillator as light source." In: (2017) (cit. on p. 6).

[17] Christoph Haisch. "Photoacoustic spectroscopy for analytical measurements." In: *Measurement Science and Technology* 23 (1 2012). DOI: 10.1088/0957-0233/23/1/012001 (cit. on pp. 6, 7).

[18] Adrás Miklós, Peter Hess, and Zoltán Bozóki. "Application of acoustic resonators in photoacoustic trace gas analysis and metrology." In: *Review of Scientific Instruments* 72 (4 2001). DOI: 10.1063/1.1353198 (cit. on pp. 7, 8, 23).

[19] Thomas Rück, Rudolf Bierl, and Frank-Michael Matysik. "Development and characterization of a laboratory setup for photoacoustic NO2 determination based on the excitation of electronic B2 and B1 states using a low-cost semiconductor laser." In: *Sensors and Actuators A: Physical* 256 (2017). DOI: 10.1016/j.sna.2017.03.024 (cit. on pp. 8, 9, 13, 23).

[20] Xukun Yin et al. "Sub-ppb nitrogen dioxide detection with a large linear dynamic rangeby use of a differential photoacoustic cell and a 3.5 W blue multimodediode laser." In: *Sensors and Actuators B: Chemical* 247 (2017). DOI: 10.1016/j.snb.2017.03.058 (cit. on p. 9).

[21] Huadan Zheng et al. "Compact photoacoustic module for methane detection incorporating interband cascade light emitting device." In: *Optics Express* 25 (14 2017). DOI: 10.1364/OE.25.016761 (cit. on pp. 9, 13).

[22] World Health Organization. *Health Aspects of Air Pollution with Particulate Matter, Ozone and Nitrogen Dioxide*. Report. WHO, 2003 (cit. on p. 9).

[23] European Environment Agency. *Air quality in Europe — 2017 report*. Report. EEA, 2017 (cit. on pp. 9, 60, 66).

[24] Hitran on the Web. URL: http://hitran.iao.ru/ (visited on 09/05/2018) (cit. on pp. 10, 11).

[25] I. T. N. Jones and Kyle D. Bayes. "Photolysis of nitrogen dioxide." In: *The Journal of Chemical Physics* 59 (9 1973). DOI: 10.1063/1.1680696 (cit. on p. 10).

[26] Huadan Zheng et al. "Ppb-level QEPAS NO2sensor by use of electrical modulationcancellation method with a high power blue LED." In: *Sensors and Actuators B: Chemical* 208 (2014). DOI: 10.1016/j.snb.2014.11.015 (cit. on p. 11).

[27] J.-M. Friedt and È. Carry. "Introduction to the quartz tuning fork." In: *American Journal of Physics* 75 (5 2007). DOI: 10.1119/1.2711826 (cit. on p. 12).

[28] J. Fonson et al. "Dual cantilever enhanced photoacoustic detector with pulsed broadband IR-source." In: *Vibrational Spectroscopy* 50 (2 2008). DOI: 10.1016/j.vibspec.2008.12.001 (cit. on p. 12).

[29] Mikko Saarinen. "Cantilever enhanced gas sensing using photoacoustic spectroscopy." Master's Thesis. Faculty of Electronics, Communications and Automation, Aalto University, 2010 (cit. on p. 12).

[30] D. Tàtrai et al. "Dual-channel photoacoustic hygrometer for airborne measurements: background, calibration, laboratory and in-flight intercomparison tests." In: *Atmosperic Measurement Techniques* 8 (1 2015). DOI: 10.5194/amt-8-33-2015 (cit. on p. 13).

[31] Justin Rouxel et al. "Miniaturized differential Helmholtz resonators for photoacoustictrace gas detection." In: *Sensors and Actuators B: Chemical* 236 (2016). DOI: 10.1016/j.snb.2016.06.074 (cit. on p. 13).

[32] Tomasz Starecki. "Analog Front-End Circuitry in Piezoelectric and Microphone Detection of Photoacoustic Signals." In: *International Journal of Thermophysics* 35 (11 2014). DOI: 10.1007/s10765-014-1715-0 (cit. on p. 13).

[33] Zürich Instruments. *Principles of lock-in detection and the state of the art*. White Paper. 2016 (cit. on p. 15).

[34] Knowles Electronics. *EK-23029-000 Microphone Outline Drawing and Performance Specification*. 2006 (cit. on p. 22).

[35] Paul Horowitz and Winfried Hill. *The Art of Electronics*. 3rd. Cambridge University Press, 2015. ISBN: 978-0521809269 (cit. on p. 28).

[36] Microchip Technology Inc. *MCP3911, 3.3V Two-Channel Analog Front End - Datasheet*. 2013. URL: http://ww1.microchip.com/downloads/en/DeviceDoc/20002286C.pdf (visited on 10/11/2018) (cit. on p. 32).

[37] Lucky A. Ishaku, David Hutson, and Des Gibson. "Temperature Effects on Photoacoustic Carbon Dioxide Sensor Developed using Mid-IR LED." In: *IEEE International Instrumentation and Measurement Technology Conference (I2MTC)*. 2018. DOI: 10.1109/I2MTC.2018.8409855 (cit. on p. 41).

[38] Semtech Corporation. *SX1272MB2xAS - Schematic*. 2016. URL: https://os.mbed.com/media/uploads/GregCr/sx1272mb2xas_e364v01a_sch.pdf (visited on 10/10/2018) (cit. on pp. 43, 64).

[39] Marco Cattani, Carlo Alberto Boano, and Kay Römer. "An Experimental Evaluation of the Reliability of LoRa Long-Range Low-Power Wireless Communication." In: *Journal of Sensors and Actuator Networks* 6 (2 2017). DOI: 10.3390/jsan6020007 (cit. on p. 43).

[40] A. Augustin et al. "A Study of LoRa: Long Range & Low Power Networks for the Internet of Things." In: *sensors* 16 (9 2016). DOI: 10.3390/s16091466 (cit. on pp. 43, 44).

[41] Linear Technology Corporation. *LTC1069-1 Low Power, 8th Order Progressive Elliptic, Lowpass Filter - Datasheet*. 1996 (cit. on p. 46).

[42] Messer. *Synthetische Luft*. 2018. URL: https://www.messer.at/documents/20556/1050335/Synth_Luft_tech.pdf/4b41b5c9-ca24-950c-1379-4ef2636a8f3a (visited on 10/06/2018) (cit. on p. 52).

[43] Philipp Breitegger and Alexander Bergmann. "A Precise Gas Dilutor Based on Binary Weighted Critical Flows to Create NO2 Concentrations." In: *Eurosensors 2018 Proceedings* (2018, accepted) (cit. on p. 52).

[44] David W. Allan. "Clock Characterization Tutorial." In: *Proceedings of the Fifteenth Annual Precise Time and Material Interval (PTTI) Applications and Planning Meeting*. 1984. URL: https://tf.nist.gov/general/pdf/2082.pdf (visited on 10/10/2018) (cit. on p. 57).

[45] STMicroelectronics. *STM32L476xx - Datasheet*. 2017 (cit. on p. 62).

[46] Semtech. *SX1272/73 860 MHz to 1020 MHz Low Power Long Range Transceiver - Datasheet*. 2017. URL: https://www.semtech.com/uploads/documents/sx1272.pdf (visited on 10/09/2018) (cit. on p. 64).

[47] Semtech Corporation. *SX1272/3/6/7/8 LoRa Modem Design Guide*. 2013. URL: https://www.semtech.com/uploads/documents/LoraLowEnergyDesign_STD.pdf (visited on 10/10/2018) (cit. on p. 64).

[48] Nuria Castell et al. "Can commercial low-cost sensor platforms contribute to air quality monitoring and exposure estimates?" In: *Environmental International* 99 (2016). DOI: 10.1016/j.envint.2016.12.007 (cit. on p. 66).

[49] Wan Jiao et al. "Community Air Sensor Network (CAIRSENSE) project: evaluation of low-cost sensor performance in a suburban environment in the southeastern United States." In: *Atmospheric Measurement Techniques* 9 (11 2016). DOI: 10.5194/amt-9-5281-2016 (cit. on p. 66).

Appendix

Appendix A.

Low-Power Wide-Area technologies as building block for smart sensors in air quality measurements

Elektrotechnik & Informationstechnik https://doi.org/10.1007/s00502-018-0639-y

ORIGINALARBEIT

Low-Power Wide-Area technologies as building block for smart sensors in air quality measurements

M. Knoll, P. Breitegger, A. Bergmann

At present, air pollution monitoring is carried out at low spatial resolution due to high costs, coming along with high accurate measurement equipment. Therefore, to expand the air pollution measurement density, data is fed into dispersion models, which only provide approximate results. To overcome this issue, a much denser sensor network is required, which is directly able to monitor air pollution values.

With the emerging technologies in the Wireless Sensor Network (WSN) area, extensive analysis of air pollution can be achieved. Especially Low-Power Wide-Area Networks (LPWAN) such as LoRa, Sigfox or NB-IoT enable smart sensing of wide areas with low power consumption.

After introducing why air pollution measurements are indispensable and which pollutants are measured, it is discussed how LPWAN enable dense spatial resolution. Subsequently, the LPWAN technologies LoRa, Sigfox or NB-IoT are introduced and compared. This is followed by distance measurements and a path loss evaluation in the urban area of Graz using LoRa, where we reached communication distances of up to 1.740 m.

Keywords: air pollution measurement; smart sensor; LPWAN; WSN; LoRa

Sensornetzwerk-Technologien als Grundlage für smarte Sensoren bei Messungen der Luftverschmutzung.

Derzeit werden Luftgütemessungen mit Hilfe von teuren, sehr genauen Messgeräten mit nur niedriger räumlicher Auflösung durchgeführt. Um die Dichte der Messwerte zu erweitern, werden Ausbreitungsmodelle verwendet, welche aber nur Resultate mit großer Schwankungsbreite liefern. Um dieses Problem zu lösen, wird ein dichteres Sensor-Netzwerk benötigt, welches direkt in der Lage ist, die Luftverschmutzung zu messen.

Mit den aufkommenden Technologien im Bereich der kabellosen Sensor-Netzwerke (engl. Wireless Sensor Network) werden großflächige Analysen der Luftverschmutzung ermöglicht. Speziell Sensornetzwerk-Technologien mit geringem Stromverbrauch (engl. Low Power Wide Area Network, LPWAN), wie zum Beispiel LoRa, Sigfox oder NB-IoT, ermöglichen eine hohe räumliche Auflösung der Sensorik.

In dieser Arbeit wird zuerst beschrieben, warum Luftgütemessungen unverzichtbar sind und welche Luftbestandteile in der Praxis gemessen werden. Anschließend wird diskutiert, wie LPWAN-Technologien hohe räumliche Auflösung ermöglichen. Weiteres werden die LPWAN-Technologien LoRa, Sigfox und NB-IoT kurz beschrieben und miteinander verglichen. Danach werden Distanzmessungen mit der LoRa-Technologie in Graz vorgestellt, bei denen Kommunikationsreichweiten bis zu 1.740 m erreicht wurden.

Schlüsselwörter: Luftgütemessungen; smarte Sensoren; LPWAN; WSN; LoRa

Received April 30, 2018, accepted July 18, 2018

1. Introduction

Air pollution is adversely affecting our environment and is known to be a huge health risk when specific limits are exceeded (cf. [1]). Pollutants are emitted from different sources, including human related (anthropogenic) and natural sources. Anthropogenic sources are mainly fuel combustion, transport, domestic heating, industry and agriculture. Currently, in the EU, twelve pollutants are measured in urban areas. Of utmost importance are the mass concentration of particulate matter (PM), of diameter smaller than 2.5 µm ($PM_{2.5}$) and smaller than 10 µm (PM_{10}) and the gases ozone (O_3), nitrogen dioxide (NO_2), sulfur dioxide (SO_2) and carbon monoxide (CO), since the permitted exceedances each year are enforced by the EU Directive 2008/50/EU [2]. The corresponding short term and long term limits are given in Table 1.

1.1 Current status of air pollution monitoring

Currently, air pollution monitoring is done at coarse spatial resolution. This is mainly because of the high costs which come along with high accurate measurement equipment and missing network technologies. In Graz and Vienna, the two biggest cities in Austria, air pollution monitoring is done with 7 and 17 measurement stations, respectively. In Vienna for example, only one measurement station per 100.000 inhabitants exists. Additionally, in many stations, not all types of pollutants are measured. Therefore, to enable air pollution

Knoll, Markus, Institute of Electronic Sensor Systems, Graz University of Technology, Inffeldgasse 10/II, 8010 Graz, Austria (E-mail: m.knoll@student.tugraz.at); **Breitegger, Philipp,** Institute of Electronic Sensor Systems, Graz University of Technology, Inffeldgasse 10/II, 8010 Graz, Austria; **Bergmann, Alexander,** Institute of Electronic Sensor Systems, Graz University of Technology, Inffeldgasse 10/II, 8010 Graz, Austria

Table 1. Air pollution limits of the most common measured pollutants specified by the EU Ambient Air Quality Directives

Pollutant	Short term limit	Long term limit
PM_{10}	50 µg/m^3 (1 day)	40 µg/m^3 (calendar year) Should not be exceeded on more than 35 days/year
$PM_{2.5}$		25 µg/m^3 (calendar year)
O_3	180 µg/m^3 (1 hour) 120 µg/m^3 (daily 8 hour mean) Should not be exceeded on more than 25 days per year averaged over 3 years	
NO_2	200 µg/m^3 (1 hour) Should not be exceeded on more than 18 hours/year	40 µg/m^3 (calendar year)
SO_2	350 µg/m^3 (1 hour) Should not be exceeded on more than 24 hours/year 125 µg/m^3 (1 day)	
CO	10 mg/m^3 (daily 8 hour mean)	

measurements at much denser spatial resolution, a different concept is required. Different concepts exist for enhancing resolution, which includes WSN – in specific LPWAN. These technologies enable high resolution sensor meshes, but also bring along disadvantages, in particular the utilization of cheap sensors with unacceptable large measurement uncertainties. The focus of this paper will be laid on network technologies. An extensive discussion on low-cost air pollution sensors can be found in [3].

1.2 What Wireless Sensor Networks (WSN) can provide

Several projects and publications exist where WSN have been used to enhance spatial resolution in air pollution monitoring. In Zurich, Hasenfratz et al. [4] created a mobile sensor network by mounting sensors on trams and busses. Data collection was implemented using the GSM network. Additionally, ozone sensors have been mounted on bicycles. Using this approach it was possible to cover an area of about 100 km^2. The CITI-SENSE project (2012–2016) [5] deployed fixed, mobile and personal nodes in eight cities in Europe. Different sensor principles and solutions for fixed and mobile nodes have been compared. Sensors showed good results in laboratory measurements, but much degraded performance in field tests, where differences in humidity and temperature had strong impacts on the measurement results. They suggested that proper sensor technology development is the requirement for spatial dense sensor networks.

In the USA, the Community Air Sensor Network (CAIRSENSE) project [6] monitored air pollution in a 2 km^2 area, using fixed stations and four wireless sensor nodes, which have been supplied by solar power and partly by AC power. Xbee radios have been used for communication, which facilitated a maximum communication range of 500 m in a suburban area. Two nodes with a distance of about 1.5 km from the base station were unable to report data via wireless communication, as messages were not received. Furthermore, strong sensor dependency on humidity and temperature has been reported with most sensors providing unreliable results. Among others, these projects show possibilities of enhancing the spatial density, whereas still problems exist in bringing together spatial density with accurate sensor resolution.

2. Low Power Wide Area Network (LPWAN) technologies

In the last years several LPWAN technologies like Sigfox, NB-IoT or LoRa have emerged. In contrast to classical WSN technologies such as ZigBee, WLAN or Bluetooth, LPWAN feature wide communication range and low power consumption, which come along with low data rates. Therefore, they cannot be used for video or audio data streaming, but are perfect fits for sensing applications, which do not need to transmit big amounts of data. The low power consumption enables battery powered device operations of up to several years. Further, the number of base stations and cost of WSN can be reduced. In the following, three major LPWAN technologies are described.

2.1 LoRa

LoRa, which stands for "long range" is a chirp spread spectrum (CSS) modulation technology [7] from Semtech Corporation. It features on the one hand the modulation scheme and on the other hand a media access control (MAC) protocol called LoRaWAN, which is promoted by the LoRa Alliance™. LoRa operates in the Industrial, Scientific and Medical (ISM) bands of 433-, 868- or 915-MHz depending on the region where it is used. Depending on the used transceiver, it is able to provide a constant RF output power of 20 dBm and data rates of up to 37.5 kbps, with the latter strongly dependent on the chosen parameters. Among others, these parameters are spreading factor (SF), bandwidth (BW) and code rate (CR). They influence data rate, communication distance and its robustness to interference. A higher spreading factor and a lower bandwidth result in higher sensitivity, but in lower data rates. The maximum sensitivity of end nodes is −146 dBm. Several publications [8–10] tested parameter settings and the resulting effects on reliability and communication distance. For instance, Augustin et al. [8] reached communication distances of up to 3.400 m in a suburban area in Paris.

As mentioned before, LoRaWAN is the MAC protocol developed by the LoRa Alliance™. The specification defines three different types of end devices, which are listed in the following. The power consumption increases from class A to class C.

Table 2. Comparison of LPWAN technologies

Attributes/Technology	LoRa (SX1276)[1]	Sigfox (S2-LPQRE)[2]	NB-IoT (SARA-N2)[2]
Frequency	Unlicensed ISM bands (433-, 868-, 915-MHz)	Unlicensed ISM bands (868 MHz, 902–920 MHz)	Licensed LTE frequency (700-, 800, -900 ... MHz)
Range	Up to several km, depending on parameters	Up to several km	Up to several km
RX sensitivity	−148 dBm	−130 dBm	−135 dBm
Data rate	37.5 kbps	600 bps	DL: 27.2 kbps/UL: 62.5 kbps
Maximum payload	255 bytes	12 bytes	1600 bytes
Power consumption	TX: 29 mA (13 dBm) RX: 12 mA	TX: 20.6 mA (14 dBm) RX: 8.6 mA	TX: 100 mA (13 dBm) RX: 46 mA
Price per transceiver (1000 pcs)	∼3,66€	∼1,26€	∼10€ (for first available transceiver)
Network Topology	Star topology, end devices do not have specific gateway	Star topology, end devices do not have specific gateway	Cellular network, end devices have specific gateway

- Class A: Uplink (from end node to the gateway/server) messages can be sent any time. Downlink windows are defined after uplink message.
- Class B: Extension of Class A with additional scheduled windows for downlink messages.
- Class C: End nodes listen always except when transmitting.

Additionally, LoRaWAN features a security stack using the Advanced Encryption Standard (AES) for secure communication and message authentication. LoRa networks can be custom built without paying substantial network fees, but the technology is protected and only the company Semtech is manufacturing LoRa ICs and distributing licenses.

2.2 Sigfox

Sigfox is an Ultra-Narrow Band (UNB) technology with binary phase shift keying (BPSK), developed by a company with the same name. In Europe, Sigfox uses the 868 MHz ISM band, while in the rest of the world the band in between 902–920 MHz. Transmission power and power consumption are similar to LoRa, with a maximum RF output of 14 dBm. The maximum data rate is specified with 600 bps, which is sufficient for most sensor applications. The network structure of Sigfox and LoRa is the same, whereby end nodes are not bound to specific gateways. Therefore, several gateways are able to receive and forward the messages, with a server or backend software responsible for filtering equal messages forwarded by multiple gateways. This approach extends the reliability of the network. The business model differs from that of the LoRa Alliance™, in which the transceiver technology is provided to silicon manufacturers. In contrast to LoRa, the network and software is sold as a service with maximum number of messages per node and day dependent on subscription level. Both uplink and downlink messages are possible, whereby downlink slots for end devices specified directly after sending message to the gateway. Currently Sigfox is covering 45 countries and an area of 3.8 million km^2 with their network.

2.3 Narrow Band-Internet of Things (NB-IoT)

Narrow-Band Internet of Things (NB-IoT) has been developed by the 3rd Generation Partnership Project (3GPP). In contradiction to LoRa and Sigfox it is deployed in authorized spectrum and is employing existing cellular (mobile) networks, which are up to now, used for human-oriented communication. The required bandwidth is 200 kHz and current GSM bands, guard bands of the LTE carrier or unused blocks in the LTE band are frequencies at which NB-IoT could be deployed. Uplink and downlink communication use different frequencies, whereas data rates are limited for uplink to 20 kbps and for downlink to 200 kbps. NB-IoT reuses and enhances the LTE protocol, while reducing the functionalities to a minimum for IoT usage. The first NB-IoT transceiver (SARA-N2) which is on the market features a maximum output power of 23 dBm and input sensitivity of −135 dBm, requiring for this setting 220 mA for transmission. Lauridsen et al. [11] compared the coverage of GPRS, NB-IoT, LoRa and Sigfox in a 7.800 km^2 area in Denmark, using radio coverage simulations, resulting in the best outcome for Sigfox and NB-IoT, especially for indoor connectivity. Apart from these simulations, real distance measurements using Sigfox or NB-IoT are not published until now.

2.4 Comparison

In Table 2, LoRa, Sigfox and NB-IoT are compared with the respect to different factors. LoRa and Sigfox are deployed in license free bands in contrary to NB-IoT, which is using licensed LTE frequency bands. Communication range cannot be directly specified, as it is very dependent on the environment. However, it is expected that all three technologies are capable of reaching several kilometers, at least in suburban areas. The maximum data rate of Sigfox (600 bps) lags behind the other two competitors, whereas the bit rate of LoRa depends on the selected PHY settings. Comparing similar output power, the SARA-N2 NB-IoT transceiver [12] requires 100 mA for 13 dBm TX power and 46 mA for RX. This is in case of transmission and listening up to five times the required power consumption of LoRa and Sigfox. Sigfox and LoRa are using star network topologies with nodes not directly linked to a specific gateway in contrast to NB-IoT. Mekki et al. [13] compared LPWAN technologies on different factors like range, battery lifetime, scalability or payload length, which showed the similarities between LoRa and Sigfox in contrary to NB-IoT.

One main limitation of LoRa and Sigfox provides the ERC Recommendation 70-03 [14] which limits the duty cycling to 1 percent (exception is one band with 10 percent) and the maximum output to 14 dBm (exception is one band with 27 dBm) in the unlicensed ISM bands.

3. Experimental evaluations using LoRa

The following chapter presents distance measurements using LoRa. Afterwards, the path loss is compared to a theoretical model. Finally

[1] Used transceiver for comparison.

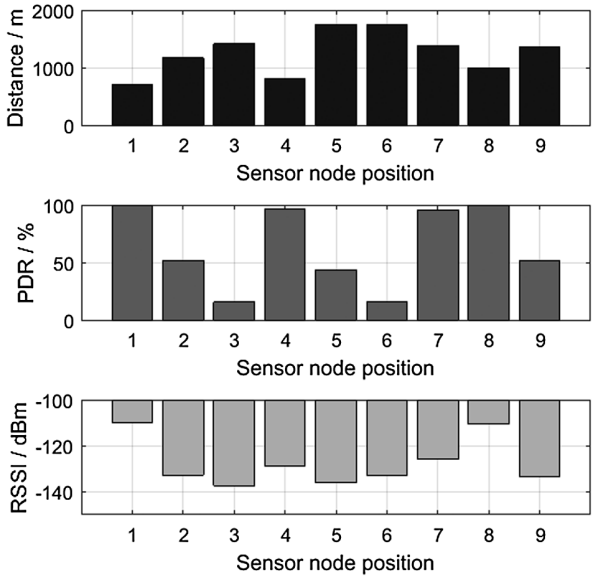

Fig. 1. Results of distance measurements for the different sensor node positions. The top plot shows the distance of the different nodes from the sink. In the second plot the packet delivery ratio from each position can be seen. In the bottom figure the averaged RSSI values from all positions are shown

Fig. 2. Map of the distance measurement showing sink, node positions (1–9) and the distance between them

the potential of the three investigated LPWAN technologies for air pollution monitoring is discussed.

The measurements were carried out in the city of Graz. For these measurements an STM32 Nucleo board with an expansion board, featuring a LoRa SX1272 transceiver, was utilized. The transceiver was used for sending (node) and receiving (sink) messages. The transceiver features a sensitivity of down to −137 dBm. Transmission power was set to a maximum of 14 dBm, which results in a maximum link budget of 157 dB, including the onboard power amplifier (PA) and the attached antenna (transmission power in total 20 dBm). In order to reach the maximum range, the LoRa parameters were set accordingly (SF = 12, BW = 125 kHz, CR = 4/8). The payload of each message contained 16 bytes including a message counter for verification. Furthermore was the transmission interval set to 4 seconds and at least 200 messages were sent per node and position. During the measurement cycle the ambient temperature was about 25 °C. In Fig. 2 the sink position, sensor node positions (1–9) and distances between these positions are shown. While the distance measurements were mainly performed in south-east districts of Graz, position 6 was located in the center of Graz. The sink was positioned on the third floor outside the window at the university campus Inffeldgasse. Further were the sensor nodes placed in a typical air pollution sensor height of 1 m.

3.1 Measurement results

The measured results are shown in Fig. 1. It was possible to receive messages from all positions. As expected, the packet delivery ratio (PDR), in which only messages without any payload error were counted, is strongly depended on the communication distance. A PDR of more than 95 percent could be achieved from four positions (1, 4, 7, 8), with distances between 710 m and 1.380 m, while the worst PDR were measured at positions 3 and 6, with 15 and 16 percent respectively. At position 5, having a distance of 1.740 m from the sink, 43 percent of the messages could be properly received. Generally speaking, the PDR correlates with the node distances, but dependency on topography and the number of buildings in between cannot be neglected.

Furthermore, the averaged RSSI values are shown in the bottom plot of Fig. 1. It becomes apparent, that the RSSI values at position 1 and 8 are significantly higher than from other positions. That can be explained by the descending terrain, which was leading to a close to line of sight (LOS) positioning. In addition to that, results a higher RSSI magnitude in a weaker signal, which indicates a higher distance. This increasing distance was leading to more packets with wrongly delivered payload.

Comparing these results to the measurements from Augustin et al. [8], only smaller distances in a more urban area have been measured. Furthermore, it has to be mentioned, that by using a more sensitive receiver like the SX1276, or a custom gateway as message sink, better results can be achieved. The reliability of the communication link can additionally be extended, by resending lost messages.

3.2 Comparison with Okumura–Hata path loss model

In this section the measured path loss is compared to the Okumura–Hata Model [15]. This relatively simple model evaluates the path loss for a certain distance between base station and a mobile sensor node. It can be seen as an extension of the free space model. The path loss in dB is thereby given as:

$$PL = A + B \cdot \log_{10}(d) + C$$

Whereby factors A, B are depending on the frequency and the antenna height (of the base station and the mobile node). The distance between the base station and mobile node is specified by d in km. Factors A and B are given using the following formulas:

$$A = 69.55 + 26.16 \cdot \log_{10}(f_c) - 13.82 \cdot \log_{10}(h_b) - a(h_m)$$

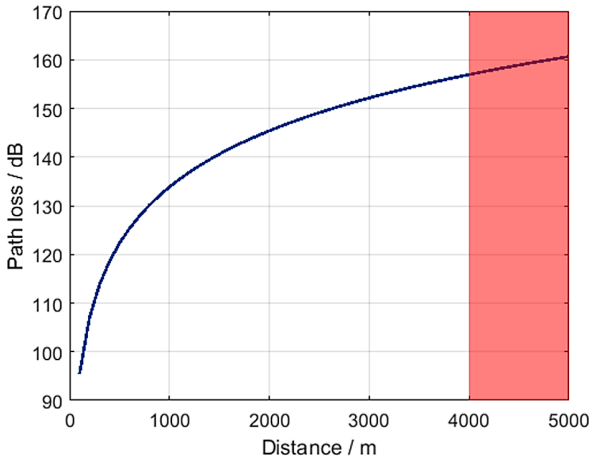

Fig. 3. Okumura–Hata Model for path loss for small and medium sized cities. The red shaded area depicts the distances which are exceeding the total link budget of the used LoRa transceiver

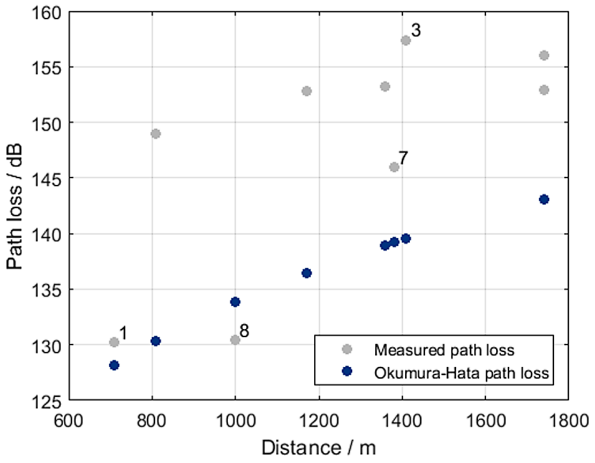

Fig. 4. Comparison of the Okumura–Hata Model for path loss and the measured path loss. Discussed measurement points are labeled

$$B = 44.9 - 6.55 \cdot \log_{10}(h_b)$$

With f_c represents the used frequency, h_b is the base station height and h_m the height of the mobile node.

Factors C and $a(h_m)$ are additionally depending on the deployed environment. For small and medium sized cities they can be calculated as followed:

$$a\left(h_m\right) = \left(1.1 \cdot \log_{10}\left(f_c\right) - 0.7\right) \cdot h_m - \left(1.56 \cdot \log_{10}(f_c) - 0.8\right)$$

$$C = 0$$

As a result, the evaluated model for distances up to 5.000 m is depicted in Fig. 3. The red shaded area represents the communication range between base station and mobile nodes, which is not usable due to insufficient link budget in case of the used LoRa SX1272 transceiver. This would result in a maximum communication distance of about 4000 m in small and medium sized cities. Figure 4 shows the model compared to the measured path loss. The measured path loss scatters due to the terrain and the obstacles in between. This cannot be represented by the simple Okumura–Hata Model, which does not include terrain profile or dominant obstacles. However it can be seen, that the measured path loss values at positions 1, 7 and 8 are well modeled by the Okumura–Hata Model. This is due to the descending area between sink and sensor position, which makes the path loss depending on the distance only. On the other hand, the modeling quality of all other positions is worse. Especially sensor position 3 shows the impact of dominant obstacles. It is directly placed behind the main building of the technical university, resulting in a weak communication link and the highest path loss. It can be concluded, that the Okumura–Hata Model is a rough indicator for the communication distance and the density of required base stations. Furthermore needs to be mentioned, that other models exist, which adjust to the area of interest (cf. [16]).

3.3 Potential utilization for air pollution monitoring

Benefits of WSNs for low cost air pollution monitoring have already been discussed in Sect. 1.2. The main limiting factors of LPWAN technologies are packet size, data rate and the limitation of maximum transmissions per hour and day. As described in the previous section, the duty cycle and therefore the transmissions per day for the ISM bands, used by Sigfox and LoRa, are limited by the EU. Sigfox additionally confines the number of transmissions by a fee-dependent subscription level. Whether these restrictions are constraining a possible deployment of LPWAN depends on the chosen sensor principle and the data evaluation mechanism. As a consequence, the following factors affect the required data transfer:

- Legislative and technological restrictions are limiting the minimum period at which the measured data can be provided.
- Depending on the sensor principle and the ambient conditions, a frequent remote sensor calibration could be necessary, which increases the required data rate.
- The data processing and evaluation can either be done at the node or at a central processing station, where the latter would significantly increase the transmissions per day.
- Additionally to the pollutant sensor data, date, timestamp and position could also be transmitted.
- If nodes are equipped with additional environmental sensors, such as temperature, humidity or other pollutants, the data rate is increasing.
- The link quality affects the number of transmission as lost or wrongly received packets might be resent.

As the discussion shows, plenty of factors affect the data transfer requirements, which is also shown by Clements et al. [17]. If the principal data evaluation can be done locally, data rate limitations should not confine the utilization of LoRa or NB-IoT. However, the previously discussed restrictions of Sigfox might limit multi-sensor platforms.

Furthermore, additional logic is required at the backend of the network for filtering redundant packets or request wrongly or lost packets. Finally, the evaluation and presentation of the received information should not be underestimated with a vast amount of data to be expected.

4. Conclusion and outlook

Overall, it can be concluded that LPWAN technologies offer promising prospects of enabling dense sensor meshes. LoRa and Sigfox bring along the required attributes including long range and small power consumption. NB-IoT is the latest technology emerging in this area and future research will show how well the technology will

perform. Additionally, NB-IoT is strongly driven by the mobile communication business, which can be an advantage compared to the other two technologies.

As mentioned in this paper a dense sensor mesh does reduce the spatial resolution, but proper sensor technology has to be used for monitoring air pollution. Otherwise the vast amount of data is redundant when specific limits cannot be reached.

Using LoRa, Graz could be covered using four to six gateways, where possibly hundreds to thousands of sensors are delivering measurement results. Still, a lot of work needs to be done, to bring sensor technologies and network capability together and form proper solutions. Next steps include the development of sensors for the criteria pollutants (NO_2, PM and Ozone), which are a.) miniaturizable, b.) energy efficient and c.) accurate enough to create useful information.

Acknowledgements

Open access funding provided by Graz University of Technology.

References

1. WHO (2000): World Health Organization, Regional Office for Europe. Available. http://www.euro.who.int/__data/assets/pdf_file/0005/74732/E71922.pdf [Accessed 26.04.2018].
2. European-Environment-Agency (2017): Air quality in Europe—2017 report. Available. https://www.eea.europa.eu/publications/air-quality-in-europe-2017 [Accessed 20.04.2017].
3. Castell, N., Dauge, F., Schneider, P., Vogt, M., Lerner, U., Fishbain, B., Broday, D., Bartonova, A. (2017): Can commercial low-cost sensor platforms contribute to air quality monitoring and exposure estimates? Environ. Int., 99, 239–302. https://doi.org/10.1016/j.envint.2016.12.007.
4. Hasenfratz, D. (2015): Enabling large-scale urban air quality monitoring with mobile sensor nodes. Dissertation. Zürich: ETH Zürich.
5. Broday, D.M., Citi-Sense-Project-Collaborators (2017): Wireless distributed environmental sensor networks for air pollution measurement—the promise and the current reality. Sensors, 17(10), 2263. https://doi.org/10.3390/s17102263.
6. Jiao, W., Hagler, G., Williams, R., Sharpe, R., Brown, R., Garver, D., Judge, R., Caudill, M., Rickard, J., Davis, M., Weinstock, L., Zimmer-Dauphinee, S., Buckley, K. (2016): Community air sensor network (CAIRSENSE) project: evaluation of low-cost sensor performance in a suburban environment in the southeastern United States. Copernicus Publications, Atoms. Meas. Tech., 9, 5281–5292. https://doi.org/10.5194/amt-9-5281-2016.
7. Semtech (2015): LoRa modulation basics. [Online]. Available: 2018. https://www.semtech.com/uploads/documents/an1200.22.pdf [Accessed: 24.04.2018].
8. Augustin, A., Yi, J., Clausen, T., Townsley, W. (2016): A study of LoRa: long range & low power networks for the Internet of things. Sensors, 17(16), 1466. https://doi.org/10.3390/s16091466.
9. Cattani, M., Boano, C. A., Römer, K. (2017): An experimental evaluation of the reliability of LoRa long-range low-power wireless communication. J. Sens. Actuators Netw., 6(2), 7. https://doi.org/10.3390/jsan6020007.
10. Centenaro, M., Vangelista, L., Zanella, A., Zorzi, M. (2016): Long-range communications in unlicensed bands: the rising stars in the IoT and smart city scenarios. IEEE Wirel. Commun., 23(5), 60–67. https://doi.org/10.1109/MWC.2016.7721743.
11. Lauridsen, M., Nguyen, H., Vejlgaard, B., Kovacs, I. Z., Preben, P., Sorensen, M. (2017): Coverage comparison of GPRS, NB-IoT, LoRa, and SigFox in a 7800 km^2 area. In VTC spring, New York: IEEE Press. https://doi.org/10.1109/VTCSpring.2017.8108182.
12. u-blox (2018): u-blox SARA-N2 datasheet. [Online] Available: https://www.u-blox.com/sites/default/files/SARA-N2_DataSheet_%28UBX-15025564%29.pdf [Accessed: 25.04.2018].
13. Mekki, K., Bajic, E., Chaxel, F., Meyer, F. (2017): A comparative study of LPWAN technologies for large-scale IoT deployment. ICT Express. https://doi.org/10.1016/j.icte.2017.12.005.
14. Electronic Communications Committee (ECC), (2017): ERC recommendation 70-03. [Online] Available: https://www.ecodocdb.dk/download/25c41779-cd6e/Rec7003%20May2018.pdf.
15. Molisch, A. F., (2011). Wirless communications, 2nd edn. Appendix, Chapter 7. [Online] Available: https://www.wiley.com/legacy/wileychi/molisch/supp2/appendices/c07_Appendices.pdf.
16. Jörke, et al. (2017): Urban channel models for smart city IoT-networks based on empirical measurements of LoRa-links at 433 and 868 MHz. In IEEE 28th annual international symposium on personal, indoor, and mobile radio communications, PMIRC. https://doi.org/10.1109/PIMRC.2017.8292708.
17. Clements, et al. (2017): Low-cost air quality monitoring tools: from research to practice (a workshop summary). Sensors, 17(11) 2478 https://doi.org/10.3390/s17112478.

Authors

Markus Knoll

received his B.Sc. degree in Telematics (now renamed to Information and Computer Engineering) from Graz University of Technology, Austria. He is currently finishing his Masters in Information and Computer Engineering at Graz University of Technology writing his master thesis about the development of a low-cost, wireless, photoacoustic based NO_2 recognition sensor for air pollution measurements. Since 2014, besides studying, he has been working at NXP Semiconductors Austria GmbH as a student employee in the verification and validation group.

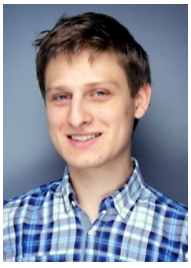

Philipp Breitegger

received his Master's degree in Technical Physics from Graz University of Technology, Austria, in 2015. He is currently pursuing his Doctoral programme in Engineering Sciences, where he is researching on high spatial resolution sensor systems for monitoring air pollutants in metropolitan areas. In 2016 he worked in a research group with focus on exhaust measurements at AVL List GmbH, before joining the Institute of Electronic Sensor Systems at Graz University of Technology as a university assistant. Since 2018 he has been chapter chair of the IEEE Austria Instrumentation and Measurement Society.

Alexander Bergmann
is head of the Institute of Electronic Sensor Systems at Graz University of Technology (TU Graz), Austria. He received his Dr. rer. nat. from the University of Graz in 2000. Afterwards he worked as assistant and assistant professor at the University of Graz. From 2000 to 2002 he was process R&D engineer at Infineon Technologies in Villach, Austria. In 2005 he joined AVL List GmbH and was working as project manager, head of development, head of research and principal scientist in the field of sensor systems. In 2016 he became a full professor at the TU Graz and founded the Institute of Electronic Sensor Systems. His research is dedicated to sensor effects, materials and smart systems for detection of gases as well as aerosols (air polluters and climate forcers) with emphasis on high temporal and spatial resolution. He has published more than 50 peer reviewed publications and 3 book chapters and fielded 25 granted patents.